

This is the accepted manuscript made available via CHORUS. The article has been published as:

Topological Magnus responses in two- and three-dimensional systems

Sanjib Kumar Das, Tanay Nag, and Snehasish Nandy

Phys. Rev. B **104**, 115420 — Published 17 September 2021

DOI: [10.1103/PhysRevB.104.115420](https://doi.org/10.1103/PhysRevB.104.115420)

Topological Magnus responses in two and three dimensional systems

Sanjib Kumar Das^{♣,1,*}, Tanay Nag^{♣,2,†} and Snehasish Nandy^{3,‡}

¹*IFW Dresden and Würzburg-Dresden Cluster of Excellence ct.qmat, Helmholtzstr. 20, 01069 Dresden, Germany*

²*Institute für Theorie der Statistischen Physik, RWTH Aachen University, 52056 Aachen, Germany*

³*Department of Physics, University of Virginia, Charlottesville, VA 22904 USA[§]*

(Dated: August 23, 2021)

Recently, time-reversal symmetric but inversion broken systems with non-trivial Berry curvature in the presence of a built-in electric field have been proposed to exhibit a new type of linear Hall effect in ballistic regime, namely, the Magnus Hall effect. The transverse current here is caused by the Magnus velocity that is proportional to the built-in electric field enabling us to examine the Magnus responses, in particular, Magnus Hall conductivity and Magnus Nernst conductivity, with chemical potential. Starting with two-dimensional (2D) topological systems, we find that warping induced asymmetry in both the Fermi surface and Berry curvature can in general enhance the Magnus response for monolayer graphene and surface states of topological insulator. The strain alone is only responsible for Magnus valley responses in monolayer graphene while warping leads to finite Magnus response there. Interestingly, on the other hand, strain can change the Fermi surface character substantially that further results in distinct behavior of Magnus transport coefficients as we observe in bilayer graphene. These responses there remain almost insensitive to warping unlike the case of monolayer graphene. Going beyond 2D systems, we also investigate the Magnus responses in three-dimensional multi-Weyl semimetals (mWSMs) to probe the effect of tilt and anisotropic nonlinear energy dispersion. Remarkably, Magnus responses can only survive for the WSMs with chiral tilt. In particular, our study indicates that the chiral (achiral) tilt engenders Magnus (Magnus valley) responses. Therefore, Magnus responses can be used as a tool to distinguish between the untilted and tilted WSMs in experiments. In addition, we find that the Magnus Hall responses get suppressed with increasing the nonlinearity associated with the band touching around multi-Weyl node.

I. INTRODUCTION

The family of Hall effects have revolutionized the solid state physics in the context of novel electronic states and electron dynamics [1–3]. Starting from the Lorentz force mediated classical Hall effect and quantum Hall effect, various new types of Hall effect such as anomalous Hall effect, spin Hall effect, thermal Hall effect etc. have been discovered over the years [1–11]. Among them, the Berry curvature (BC) induced Hall effects, taking place without external magnetic field, have drawn tremendous attention to both the theorists and experimentalists [4–10, 12]. For time reversal symmetry (TRS) broken systems, the BC takes the form $\Omega(\mathbf{k}) \neq -\Omega(-\mathbf{k})$ leading to a finite total BC for the occupied states. By contrast, in TRS invariant systems, BC follows $\Omega(\mathbf{k}) = -\Omega(-\mathbf{k})$ giving rise to zero total BC [12], that further causes the intrinsic anomalous Hall effect to vanish. Interestingly, it has been theoretically proposed and experimentally verified that unlike the linear anomalous Hall effect, the nonlinear anomalous Hall effect can survive in TRS invariant systems with broken inversion symmetry [13–21]. Very recently, the same systems (TRS invariant but inversion broken) with a built-in electric field at zero magnetic field is found to exhibit a new type of a linear response namely,

Magnus Hall effect (MHE) [22]. The MHE is originated from the Magnus velocity of electron that is perpendicular to the BC and the built-in electric field. Along with the prediction of MHE, it has also been proposed that the Magnus Nernst effect (MNE) and Magnus thermal Hall effect can also appear in these systems in the presence of applied thermal gradient [23].

It has been proposed that the two-dimensional (2D) transition metal dichalcogenides MX_2 (M=Mo, W and X=S, Se, Te) [14, 24–26], monolayer (ML) graphene on hBN, bilayer (BL) graphene with applied perpendicular electric field [27–29], heterostructures [30] and surfaces of topological insulator (TI) [31] are the possible candidates to investigate the MHE and MNE for their TRS invariant and inversion broken nature. The MHE has been theoretically studied recently in graphene and transition metal dichalcogenides using the low-energy model without warping (except bilayer graphene where trigonal warping is considered) and strain [22, 23]. On the other hand, it has been shown that without spin-orbit coupling and tilting of Dirac cone, the BC dipole becomes substantially large in presence of strain and warping for graphene [29]. Motivated by the BC dipole induced nonlinear anomalous Hall effect in TRS invariant systems, our interest here is to investigate Magnus transport in the presence of strain and warping for the above proposed suitable candidates.

Turning to the field of three-dimensional (3D) topological systems such as, Weyl semimetals (WSMs), considered to be a 3D analogue of graphene, have been studied extensively for their intriguing properties and anomalous

* s.k.das@ifw-dresden.de

† tnag@physik.rwth-aachen.de

‡ sn5jm@virginia.edu

§ ♣ Both authors SKD and TN contributed equally.

response functions. The gap closing points, guaranteed by some crystalline symmetries, in WSMs are referred to as Weyl nodes with topological charge $n = 1$ [32–38]. There exists two Weyl nodes of opposite chiralities for the TRS broken WSM, while inversion broken WSM exhibits at least four Weyl nodes [39, 40]. The WSMs can also be classified as type-I and type-II. In the case of type-I WSM, Fermi surface is always point like irrespective of the tilting of the node. On the other hand, in type-II WSM finite electron and hole pockets appear at the Fermi level as a result of finite tilting of the energy spectra [41–43]. Moreover, it has been recently found that $n > 1$ multi-WSM (mWSM) shows non-linear band touching [44, 45]. The WSMs are shown to exhibit many intriguing transport properties, originated by chiral anomaly, such as negative longitudinal magnetoresistance and planar Hall effect [46–59]. Tilting of energy dispersion and non-linearity of band touching further decorate the transport signatures [60–64]. This motivates us to extend our investigation of MHE to 3D topological systems considering a generic mWSM Hamiltonian.

In this work, we first capture intriguing Fermi surface phenomena in presence of strain and warping by examining MHE and MNE in ballistic regime for 2D topological systems such as, ML, BL graphene and surface states of TIs. We find that in strained ML graphene without warping, the total valley integrated Magnus responses are zero as the contribution coming from individual valley exactly cancels each other. The valley polarized contribution thus leads to the Magnus valley Hall, Magnus valley Nernst effects. Interestingly, warping induces valley integrated finite Magnus responses as the asymmetries in Fermi surface and BC result in unequal valley polarized contributions. The magnitude of the Magnus responses enhance with increasing the warping parameter. The same is observed for the surface states of TI in presence of hexagonal warping. On the other hand, for BL graphene, the Magnus transport coefficients are substantially modified depending on the positive and negative values of strain while warping do not affect the Magnus transport. Finally, going beyond 2D systems, we study Magnus responses in 3D WSMs to examine the effect of tilt and anisotropic nonlinear dispersion. We find that the MHE is identically zero for each Weyl node without tilt. Remarkably, chiral (achiral) tilt causes finite MH and MN conductivities to generate from individual Weyl nodes resulting in Magnus (Magnus Valley) responses. Moreover, our study indicates that the topological charge associated with Weyl node imprints its effect on the Magnus transport properties.

The rest of the paper is organized as follows. In Sec. II, we derive the general expressions of MH and MN conductivities in both ballistic and diffusive regimes. Following which, in sec. III we have calculated the Magnus transport responses in the presence of strain and warping (tilt and non-linearity) for different 2D (3D) topological systems, respectively. Finally, we summarize our results and discuss possible future directions in Sec. IV.

II. FORMALISM OF MAGNUS TRANSPORT

In this section, we derive the general expression for MH, MN conductivities in both diffusive and ballistic regimes using Boltzmann transport equation. To begin with, we consider mesoscopic systems of electronic transport in a Hall bar device without applying any external magnetic field. In this setup, the source and the drain are kept at different electrostatic potential energy with the gate voltages given by U_s and U_d , respectively. Their difference $\Delta U = U_s - U_d$ introduces a built-in electric field $\mathbf{E}_{in} = \nabla_{\mathbf{r}}U/e$ ($-e$ is the electronic charge) in the device with a slowly varying electric potential energy $U(r)$ along the length of the sample.

Now in the presence of external electric field \mathbf{E} and temperature gradient $\nabla \mathbf{T}$ applied between the source and drain, the charge current \mathbf{J} and thermal current \mathbf{Q} from linear response theory, can be written as

$$\begin{aligned} J_a &= \sigma_{ab}E_b + \alpha_{ab}(-\nabla_b T) \\ Q_a &= \bar{\alpha}_{ab}E_b + \kappa_{ab}(-\nabla_b T), \end{aligned} \quad (1)$$

where a and b are spatial indices running over x, y, z . Here σ, α and κ different conductivity tensors.

The phenomenological Boltzmann transport equation can be written as [65, 66]

$$\left(\frac{\partial}{\partial t} + \dot{\mathbf{r}} \cdot \nabla_{\mathbf{r}} + \dot{\mathbf{k}} \cdot \nabla_{\mathbf{k}} \right) f_{\mathbf{k},\mathbf{r},t} = I_{coll}\{f_{\mathbf{k},\mathbf{r},t}\}, \quad (2)$$

where the right side $I_{coll}\{f_{\mathbf{k},\mathbf{r},t}\}$ is the collision integral which incorporates the effects of electron correlations and impurity scattering. The electron distribution function is denoted by $f_{\mathbf{k},\mathbf{r},t}$. Now under the relaxation time approximation the steady-state Boltzmann equation can be written as

$$(\dot{\mathbf{r}} \cdot \nabla_{\mathbf{r}} + \dot{\mathbf{k}} \cdot \nabla_{\mathbf{k}})f_{\mathbf{k}} = \frac{f_0 - f_{\mathbf{k}}}{\tau(\mathbf{k})}, \quad (3)$$

where $\tau(\mathbf{k})$ is the scattering time. Note that in this work, we ignore the momentum dependence of $\tau(\mathbf{k})$ for simplifying the calculations and assume it to be a constant. The equilibrium distribution function f_0 in absence of applied electric field \mathbf{E} and temperature gradient $\nabla_r T$ is given by the Fermi function,

$$f_0(\mathbf{k}, \mathbf{r}) = \frac{1}{1 + e^{\beta[\epsilon(\mathbf{k}, \mathbf{r}) - \mu]}}, \quad (4)$$

where $\beta = 1/(k_B T)$, $\epsilon(\mathbf{k}, \mathbf{r}) = \epsilon_{\mathbf{k}} + U(\mathbf{r})$, with $\epsilon_{\mathbf{k}}$ and μ are the energy dispersion and chemical potential, respectively. The motion of the wave packet inside the Hall bar is described by the semiclassical equations of motion [67, 68]

$$\hbar \dot{\mathbf{r}} = \nabla_{\mathbf{k}} \epsilon_{\mathbf{k}} + [\nabla_{\mathbf{r}} U + e\mathbf{E}] \times \boldsymbol{\Omega}, \quad (5)$$

$$\hbar \dot{\mathbf{k}} = -\nabla_{\mathbf{r}} U - e\mathbf{E}. \quad (6)$$

The first, second and third term in the right hand side of Eq. (5) respectively represent the band velocity, Magnus velocity $V_{\text{magnus}} = \nabla_{\mathbf{r}} U \times \boldsymbol{\Omega}$ and anomalous velocity

$V_{\text{ano}} = \mathbf{E} \times \boldsymbol{\Omega}$. The Magnus velocity V_{magnus} can be thought of a quantum analog of the classical Magnus effect.

Now to calculate MH and MN conductivities, we apply the electric field and temperature gradient along x direction. Assuming the length of the sample is along x axis, we have $U(\mathbf{r}) = U(x)$, $\epsilon(\mathbf{k}, \mathbf{r}) = \epsilon_{\mathbf{k}} + U(x)$ and $\mathbf{E}_{\text{in}} = \frac{1}{e} \frac{\partial U(x)}{\partial x} \hat{x}$. Since we consider $U(x)$ is slowly varying, the electron wave packets traveling inside the sample still have well-defined momentum \mathbf{k} . Considering the velocity of an incident electron (v_x, v_y) , transit time through the electric field region becomes $t = L/v_x$ where L is device length along x -direction. For $v_y \neq 0$, the center of the wave packet receives a transverse shift (in y -direction), followed by Magnus velocity proportional to $\nabla_x U \Omega_z$, while traversing the junction due to the built-in electric field \mathbf{E}_{in} . Now the charge and thermal currents can be written as

$$\{\mathbf{J}(x), \mathbf{Q}(x)\} = \int d\mathbf{k} \, \dot{\mathbf{r}} \{-e, [\epsilon(\mathbf{k}, x) - \mu]\} f(\mathbf{k}, x). \quad (7)$$

Combining Eqs. (3), (5), and (6) the non-equilibrium distribution function f up to linear order in the bias fields can be written as

$$f = f_0 + v_x \tau \left(eE_x + \frac{[\epsilon(\mathbf{k}, \mathbf{r}) - \mu]}{T} \nabla_x T \right) \partial_{\epsilon} f_0. \quad (8)$$

Considering U as a slowly varying function of x , $\partial U / \partial x = \Delta U / L$, one can obtain f to be spatially independent. To be precise, using Eq. (8) into the Eq. (7) and comparing with Eq. (1), the MH conductivity σ is found to be [23]

$$\sigma = -\frac{e^2 \tau}{\hbar} \frac{\Delta U}{L} \int d\mathbf{k} \, \Omega_z v_x \partial_{\epsilon} f_0, \quad (9)$$

Similarly, the MN conductivity α is given by [23]

$$\alpha = \frac{ek_B \tau}{\hbar} \frac{\Delta U}{L} \int d\mathbf{k} \, \Omega_z v_x \beta (\epsilon_{\mathbf{k}} - \mu) \partial_{\epsilon} f_0 \quad (10)$$

where we have neglected the contributions coming from the band velocity. Interestingly, as discussed above these Magnus responses are dependent on the built-in electric field.

Considering the limit $\mu \gg \frac{1}{\beta}$ in Eq. (9)-(10), the Wiedemann-Franz law and Mott relation allow us to compute MN conductivity α and Magnus thermal Hall (MTH) conductivity κ alternatively [65, 69, 70]

$$\alpha = -\frac{\pi^2 k_B^2 T}{3e} \frac{\partial \sigma}{\partial \mu}, \quad \text{and} \quad \kappa = \frac{\pi^2 k_B^2 T}{3e^2} \sigma. \quad (11)$$

Having discussed above the diffusive limit, we shall now illustrate the Magnus responses in the ballistic regime. Since in this regime, the mean free time between two collisions is infinite $\tau \rightarrow \infty$ i.e., essentially no collision occur in the transport direction inside the length L along the x -direction of the Hall bar. Therefore, the right hand side of the Boltzmann transport equation given in

Eq. (2) vanishes in the ballistic regime. In this setup, the carriers from the source with only positive velocity $v_x > 0$ are allowed in region $0 < x < L$. Now the ansatz for the non-equilibrium distribution function is the following

$$f(\mathbf{k}, \mathbf{r}) = \begin{cases} -\Delta \mu \partial_{\epsilon} f_0 - \frac{\epsilon(\mathbf{k}, \mathbf{r}) - \mu}{T} \Delta T \partial_{\epsilon} f_0 & \text{for } v_x > 0, \\ 0 & \text{for } v_x < 0. \end{cases} \quad (12)$$

Comparing the Eq. (8) and Eq. (12), one can identify the scattering length $v_x \tau$ with the device length L so that $-eLE_x = \Delta \mu$ and $\Delta T / L = -\nabla_x T$. The MH and MN coefficients in ballistic regime can be obtained as [22, 23]

$$\sigma = -\frac{e^2}{\hbar} \Delta U \int_{v_x > 0} d\mathbf{k} \, \Omega_z \partial_{\epsilon} f_0, \quad (13)$$

$$\alpha = \frac{e}{\hbar T} \Delta U \int_{v_x > 0} d\mathbf{k} \, \Omega_z (\epsilon_{\mathbf{k}} - \mu) \partial_{\epsilon} f_0. \quad (14)$$

Similar to the diffusive regime, the Magnus transport coefficients in the ballistic regime also obey the Mott relation and the Wiedemann-Franz law.

We would now like to add a few comments on Magnus responses. It is clear from the Eqs. (9)-(10) as well as Eqs. (13)-(14) that the MHE and MNE are purely determined by Fermi surface properties as they incorporate $\partial_{\epsilon} f_0$ factor. In order to obtain finite Magnus responses, the systems should have asymmetric Fermi surface. In addition, the system must possess finite BC. Moreover, the condition $v_x > 0$ happens to be very important while summing the BC over the Brillouin zone. Combining all these, the active momentum modes \mathbf{k}_v , over the Fermi surface $\epsilon_{\mathbf{k}} = \mu$, for which $v_x > 0$ would contribute to Magnus transport. The remaining momentum modes $\mathbf{k} - \mathbf{k}_v$ become inert in this ballistic transport and BC for these momentum modes do not determine the transport. These transports thus allow us to scan different Fermi surfaces by tuning μ and get the idea about angular distribution of BC within a given Fermi surface.

The Magnus responses can be regarded as an effective second order transport as the built-in electric field ΔU and external bias both come into calculation of currents. However, in terms of the external bias field, it is still a linear response phenomena. The BC dipole induced second order transport [13], given by $D_{ij} = \int d\mathbf{k} \, d_{ij} \delta(\epsilon_{\mathbf{k}} - \mu)$ with $d_{ij} = v_i(\mathbf{k}) \Omega_j(\mathbf{k})$, is primarily different from Magnus transport for which the tilting of Dirac cone is no longer important to obtain a finite response. Depending upon the mirror symmetries present in the systems, one can find symmetry permitted components of non-linear transport coefficients where d_{ij} becomes an even function of \mathbf{k} [17, 71, 72]. By contrast, quantized non-linear response namely, circular photo-galvanic effect can be observed for mirror symmetry broken non-centrosymmetric systems [73, 74].

Regarding the symmetry requirements to observe Magnus ballistic transport, we note that the presence of

crystalline symmetries such as in-plane C_2 and out-of-plane mirror can generate clean MH responses, nullifying other trivial linear transverse signals [75]. Using these crystalline symmetries, it is also possible to categorize non-linear anomalous Hall and Magnus Hall effects in different classes of material, in which time-reversal symmetry is preserved but inversion is broken. To be more precise, the noncentrosymmetric point groups containing $\{C_{2z}, C_{4z}, C_{6z}, S_{4z}\}$ symmetry operations force the BC to become zero, and as a consequence both MH conductivity and non-linear Hall conductivity both vanish in these systems. Following the above analysis, crystallographic point groups $\{C_1, C_{1h}, C_{1v}, C_2, C_{2v}, C_3, C_{3h}, C_{3v}, D_{3h}, D_3\}$ (2D transition metal dichalcogenides such as, WTe_2 , MoS_2) and $\{O, T, T_h\}$ (particularly for 3D) allowing non-zero local BC can lead to both MHE and non-linear Hall effect in general [13, 75].

We would also like to point out that at least one symmetry between TRS and inversion symmetry has to be broken in the system. Although the previous studies only concentrate on TR invariant and inversion symmetry broken systems, one can in principle get Magnus responses even in the absence of TRS as long as the active momentum modes over the Fermi surface have finite BC. This further motivates us to study TRS broken topological systems in addition to the TRS invariant topological systems. Since the strain, warping, and tilt can modify the Fermi surface significantly as well as the BC distribution accordingly, the Magnus responses can show interesting behavior which we discuss in next section.

It is important to note that along with Magnus Hall current, there exists a trivial transverse current (regular Hall current) that arises from the transverse velocity anisotropy of the Fermi surface: $\int_{v_x > 0} d\mathbf{k} v_y(\mathbf{k}) \delta(\epsilon_{\mathbf{k}} - \mu)$. However, according to the symmetry analysis given above, in presence of certain mirror symmetry (specifically, mirror plane perpendicular to the current direction) combined with time reversal symmetry, the trivial transverse current can be shown to vanish leaving a finite MH current[22, 75]. In addition to the trivial Hall current, linear anomalous Hall current induced by the non-trivial BC can appear simultaneously with MHE in time-reversal broken systems. However, in contrast to MHE, linear anomalous Hall response is not a Fermi surface phenomenon and therefore, does not depend on the derivative of the Fermi function. These two effects can be distinguished by looking at their chemical potential dependencies in experiments. We will discuss these issues elaborately in Sec. III D.

III. RESULTS

In this section, we discuss the effect of strain and warping on MH and MN conductivities in inversion symmetry broken but TRS invariant 2D topological systems, namely for ML, BL graphene and surface states of TI.

We extend our analysis in 3D topological systems WSMs, breaking either TRS or inversion symmetry, to investigate the effect of tilt and non-linearity on MHE and MNE. At the outset, we note that we will often refer MH and MN conductivities together as MH responses.

A. Strained monolayer graphene

The graphene hosts gapless Dirac cones, located at the high symmetry points \mathbf{K} and \mathbf{K}' in the Brillouin zone, with vanishing BC. A finite BC is generated by breaking the inversion symmetry that can be engineered by placing the graphene sheet on hBN substrate[76, 77]. This actually reduces the point group of the system from C_{6v} to C_{3v} , and opens up a gap at the Dirac nodes. Upon applying a uniform uniaxial strain along one of the two main crystallographic directions in graphene, the massive Dirac nodes become shifted from the high symmetry points along the $k_y = 0$ line due to the combination of TRS and mirror symmetry. The application of the strain creates a difference between hopping amplitudes along the two main crystallographic directions and therefore, changes the corresponding Fermi velocities[29, 78].

Considering only first-order momentum-strain coupling, the low-energy Hamiltonian of the ML strained graphene can be written as [29]

$$\mathcal{H}_0^{ML}(\mathbf{k}) = \frac{\Delta_g}{2} \sigma_z + \zeta v_1 k_x \sigma_x + v_2 k_y \sigma_y, \quad (15)$$

where v_1 and $v_2 \neq v_1$ are two strain-dependent Fermi velocities along x and y directions respectively, Δ_g is the gap (also called Semenoff mass), ζ is the valley index and σ 's represent Pauli matrices incorporating sublattice degrees of freedom. To introduce the warping effect in the system, we add a trigonal warping terms, proportional to k^2 , in the Hamiltonian (15). Even though the magnitude of the warping term is smaller compared to the leading order term in k , it plays a crucial role in MH responses. Now the complete Hamiltonian for the ML graphene in the presence of both uniaxial strain and trigonal warping reads as [29];

$$\begin{aligned} \mathcal{H}^{ML}(\mathbf{k}) = & \frac{\Delta_g}{2} \sigma_z + \zeta v_1 k_x \sigma_x + v_2 k_y \sigma_y + 2\zeta \lambda_3 k_x k_y \sigma_y \\ & + (\lambda_1 k_y^2 - \lambda_2 k_x^2) \sigma_x = \mathbf{N}_{\mathbf{k}} \cdot \boldsymbol{\sigma} \end{aligned} \quad (16)$$

with $\mathbf{N}_{\mathbf{k}} = \{\mathbf{N}_{1\mathbf{k}}, \mathbf{N}_{2\mathbf{k}}, \mathbf{N}_{3\mathbf{k}}\} = \{\zeta v_1 k_x + (\lambda_1 k_y^2 - \lambda_2 k_x^2), v_2 k_y + 2\zeta \lambda_3 k_x k_y, \frac{\Delta_g}{2}\}$ and $\boldsymbol{\sigma} = \{\sigma_1, \sigma_2, \sigma_3\}$. Here, λ_1 , λ_2 and λ_3 are the warping terms. The energy dispersion of the Hamiltonian for $\zeta = \pm 1$ valley is given by

$$E^{ML}(\mathbf{k}) = |\mathbf{N}_{\mathbf{k}}| = \pm \sqrt{\mathbf{N}_{1\mathbf{k}}^2 + \mathbf{N}_{2\mathbf{k}}^2 + \mathbf{N}_{3\mathbf{k}}^2} \quad (17)$$

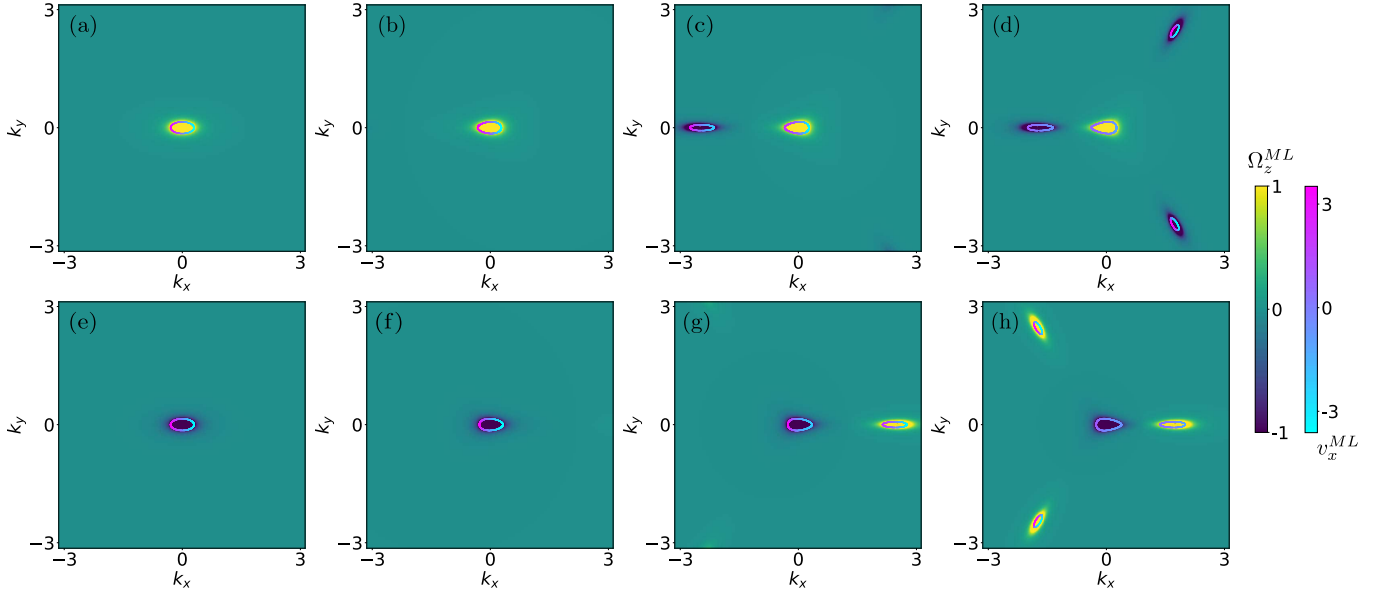


Figure 1. The evolution of BC and Fermi surface in ML graphene (16) with warping $\lambda_1 = \lambda_2 = \lambda_3 = \lambda$ and strain $v_2 \neq v_1$. Top panel: The BC ($\Omega_z^{ML}(\mathbf{k}, \zeta = +1)$) and x component of the velocity ($v_x^{ML}(\mathbf{k}, \zeta = +1)$) over the Fermi surface are shown for (a) unstrained ML graphene without warping ($v_2 = v_1$, $\lambda = 0$), and strained ML graphene ($v_2 = 2v_1$) with C_3 symmetric warping of different strengths (b) $\lambda = 0.2$, (c) $\lambda = 0.35$, (d) $\lambda = 0.5 \text{ eV} \cdot \text{\AA}^2$. Bottom panel: (e)-(h) depict $\Omega_z^{ML}(\mathbf{k}, \zeta = -1)$ and $v_x^{ML}(\mathbf{k}, \zeta = -1)$. The strength of $\Omega_z^{ML}(\mathbf{k}, \zeta)$ and $v_x^{ML}(\mathbf{k}, \zeta)$ are represented in the color codes side by side. The parameters (in the units of energy eV) used in the calculations are $\Delta_g = 0.06 \text{ eV}$, $v_1 = 0.87 \text{ eV} \cdot \text{\AA}$. The Fermi surface is plotted for the constant energy $E = -0.28 \text{ eV}$.

where $+$ ($-$) represents conduction (valence) band. The warping results in non-linearity and strain causes anisotropy in the dispersion. The BC reads as

$$\Omega_a(\mathbf{k}) = \epsilon_{abc} \frac{\mathbf{N}_k \cdot \left(\frac{\partial \mathbf{N}_k}{\partial k_b} \times \frac{\partial \mathbf{N}_k}{\partial k_c} \right)}{4|\mathbf{N}_k|^3} \quad (18)$$

where ϵ_{abc} is the usual Levi-Civita symbol.

Since ML graphene is a two-dimensional system, only z component of the BC is nonzero. Using Eq. (18), the BC for strained ML graphene ($\zeta = \pm 1$) given in Eq. (16) can be calculated as

$$\Omega_z^{ML}(\mathbf{k}, \zeta) = \pm \frac{\Delta_g [\zeta v_1 v_2 + 2k_x (\lambda_3 v_1 - \lambda_2 v_2) - 4\zeta \lambda_3 (\lambda_2 k_x^2 + \lambda_1 k_y^2)]}{4(E^{ML}(\mathbf{k}))^3} \quad (19)$$

where $+$ ($-$) represents conduction (valence) band. Now the x component of the velocity of ML graphene can be written as

$$v_x^{ML}(\mathbf{k}, \zeta) = \pm \frac{2\zeta \lambda_3 k_y \mathbf{N}_{2\mathbf{k}} + \mathbf{N}_{1\mathbf{k}} (\zeta v_1 - 2\lambda_2 k_x)}{E^{ML}(\mathbf{k})}. \quad (20)$$

We first consider strained ML graphene $v_1 \neq v_2$ without warping i.e., $\lambda_1 = \lambda_2 = \lambda_3 = 0$. It is then clear from the Eq. (19) that the BC at two different valleys

($\zeta = \pm 1$) become opposite of each other for both pristine as well as strained ML graphene i.e., $\Omega_z^{ML}(\mathbf{K}, \zeta = +1) = -\Omega_z^{ML}(\mathbf{K}', \zeta = -1)$. Moreover, the BC in this case is directly proportional to the bandgap of the system. On the other hand, $v_x^{ML}(\mathbf{K}, \zeta = +1) = v_x^{ML}(\mathbf{K}', \zeta = -1)$ as evident from Eq. (20).

The above discussion refers to the fact that there exists equal number of \mathbf{k} -modes for which $v_x^{ML} > 0$ with both signs of $\Omega(\mathbf{k})$ in each valley. Upon the momentum integration followed by Eqs. (13)-(14), the MH and MN conductivities for each valley in ballistic regime can be obtained as

$$\sigma_\zeta = \zeta \frac{\Delta_g e^2}{8\hbar\pi\mu^2} \Delta U, \quad \alpha_\zeta = \zeta \frac{\Delta_g \pi K_B^2 T e}{12\hbar\mu^3} \Delta U. \quad (21)$$

Interestingly, the above conductivities are independent of velocities v_1 and v_2 . This leads to the fact that the uniaxial strain does not affect the MH responses in ML graphene in absence of warping $\lambda_{1,2,3} = 0$. Moreover, it is also clear from Eq. (21) that the contributions of MH and MN conductivities for two valleys ($\zeta = \pm 1$) are equal and opposite. Therefore, summing over the valleys ($\zeta = \pm 1$), the total MH responses vanishes in the strained ML graphene without λ 's, similar to the case of pristine ML graphene. Instead the valley polarized transport can lead to Magnus valley Hall and Magnus valley Nernst effects where the electrons with opposite valley index accumulate on the different edges of the sample [79–81]. To be precise, consider a ML graphene system (with $\lambda_{1,2,3} = 0$) with chemical potential $(\mu + \delta\mu/2)$,

$(\mu - \delta\mu/2)$ at the $\zeta = \pm 1$ valleys respectively, the total Magnus valley Hall conductivity will be finite and takes the form $\sigma_{\text{valley}} = \sum_{\zeta} \sigma_{\zeta}(\mu + \zeta\delta\mu/2) \simeq \frac{\Delta_g}{4\hbar\pi\mu^3} \frac{e^2\Delta U\delta\mu}{4\hbar\mu^3}$. Similarly, Magnus valley Nernst conductivity is given by $\alpha_{\text{valley}} = \sum_{\zeta} \alpha_{\zeta}(\mu + \zeta\delta\mu/2) \simeq \frac{\Delta_g\pi K_B^2 T e\Delta U\delta\mu}{4\hbar\mu^4}$. We note that in order to observe the above valley polarized ballistic Magnus response, the dimension of the system has to be smaller or comparable to the mean free path.

We shall now discuss the effect of C_3 symmetric warping in MH responses by considering $\lambda_1 = \lambda_2 = \lambda_3 = \lambda \neq 0$. It is clear from the Eq. (19) and (20) that the BC and velocity of each valley are not equal and opposite compared to unwarped case. The evolution of BC and v_x^{ML} for different strength of λ are depicted in Fig. 1 (b)-(d) and Fig. 1 (f)-(h) for $\zeta = 1$ and $\zeta = -1$ valleys, respectively. The warping terms introduce satellite Dirac cones with $\theta \rightarrow \theta + 2n\pi/3$ (with $n = 1, 2, 3$) appearing around each Dirac points [82]; here $\theta = \pi$ (0) for valleys $\zeta = +1$ (-1). These additional satellite Dirac cones appear with opposite chirality as compared to that of the parent Dirac cone. The important point to note here is that the relative strength between v_1 and v_2 determines the distance of satellite Dirac points from the parent Dirac point. For example, $v_1 > v_2$ ($v_1 < v_2$) would cause the satellite Dirac points to move more (less) in k_x direction more (less) than k_y direction.

Following the above discussion, it is evident that each valley of ML strained graphene in the presence of warping does not contribute to MH and MN conductivities in an equal and opposite manner that we found for strained ML graphene. As a result, the non-zero MH responses are directly observed by summing over the contribution for both the valleys. The warping results in non-linear and anisotropic dispersion as shown in Eq. (17). As a result, BC becomes anisotropic and exhibits rich features over the Fermi surface (see Fig. 1). Since the expressions of BC and velocity of ML graphene in the presence of warping are quite complicated, it is very difficult to calculate MH and MN conductivities analytically. Therefore, below we have calculated Magnus responses numerically to investigate in detail.

The valley integrated MH and MN conductivities as a function of chemical potential (μ) are shown in Fig. 2 (a) and (b), respectively. We find that the magnitude of both transport coefficients enhances with the increase of warping strength for a fixed strain. The window of activated momentum modes over the Fermi surface changes with warping strength. Moreover, band bending imprints its signature through the Fermi surface distribution. All these lead to the intriguing behavior of the response coefficients. We find that MH responses show significant different behaviors for $v_1 > v_2$ as compared to $v_2 > v_1$. This refers to fact that the strain becomes instrumental in controlling the response in presence of warping terms. We would like to point out that the MH and MN conductivities can acquire both positive and negative values. This is due to the fact that the BC around the additional

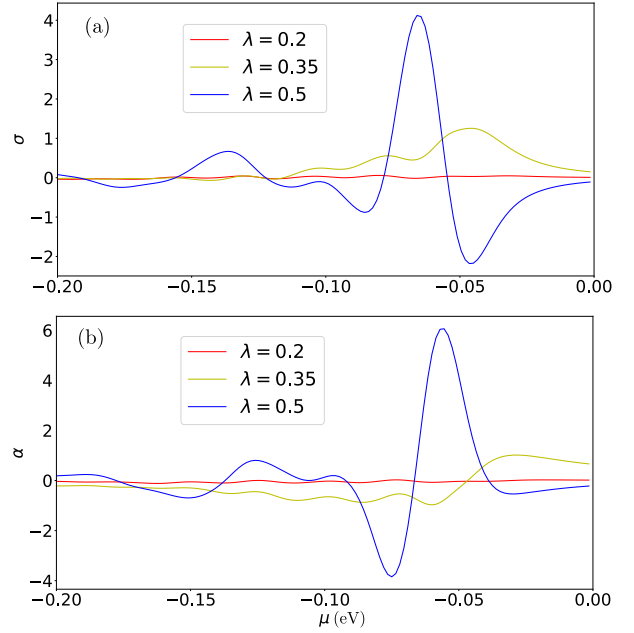


Figure 2. The total valley summed contributions of (a) MH conductivity σ (in the unit of $10^{-3}e^2/h$) and (b) MN conductivity α (in the unit of $10^{-5}ek_B/h$) in the presence of strain ($v_2 = 2v_1$) for different warping strengths $\lambda = 0.2, 0.35$ and $0.5 \text{ eV}\cdot\text{\AA}^2$ are shown for ML graphene. Noticeably, the warping can enhance the responses even after valley sum is performed, as it generates asymmetric contributions between valleys. We consider $\Delta U = 0.01 \text{ eV}$ and $k_B T = 0.001 \text{ eV}$. All other parameters are kept same as that of in Fig. 1. The chemical potential μ is chosen in the unit of eV throughout the paper.

satellite Dirac points take opposite values as compared to that of the for the parent Dirac point. These are the markedly different responses while the warping terms are introduced in the ML strained graphene. Our study further supports that the Mott relation can successfully describe MN conductivity from MH conductivity even in the presence of warping.

In summary, for monolayer graphene without strain and warping, the MH and MN conductivities for two valleys are equal and opposite, and therefore, summing over the valleys, the total MH responses vanishes [23]. On the other hand, we show that each valley of monolayer strained graphene in the presence of warping does not contribute to MH and MN conductivities in an equal and opposite manner, and hence lead to a finite valley integrated MH response. This happens because the warping results in non-linear and anisotropic dispersion as shown in Eq. (17). As a result, BC becomes anisotropic and exhibits rich features over the Fermi surface.

B. Strained bilayer graphene

The BL graphene belongs to the D_{3d} point group sym-

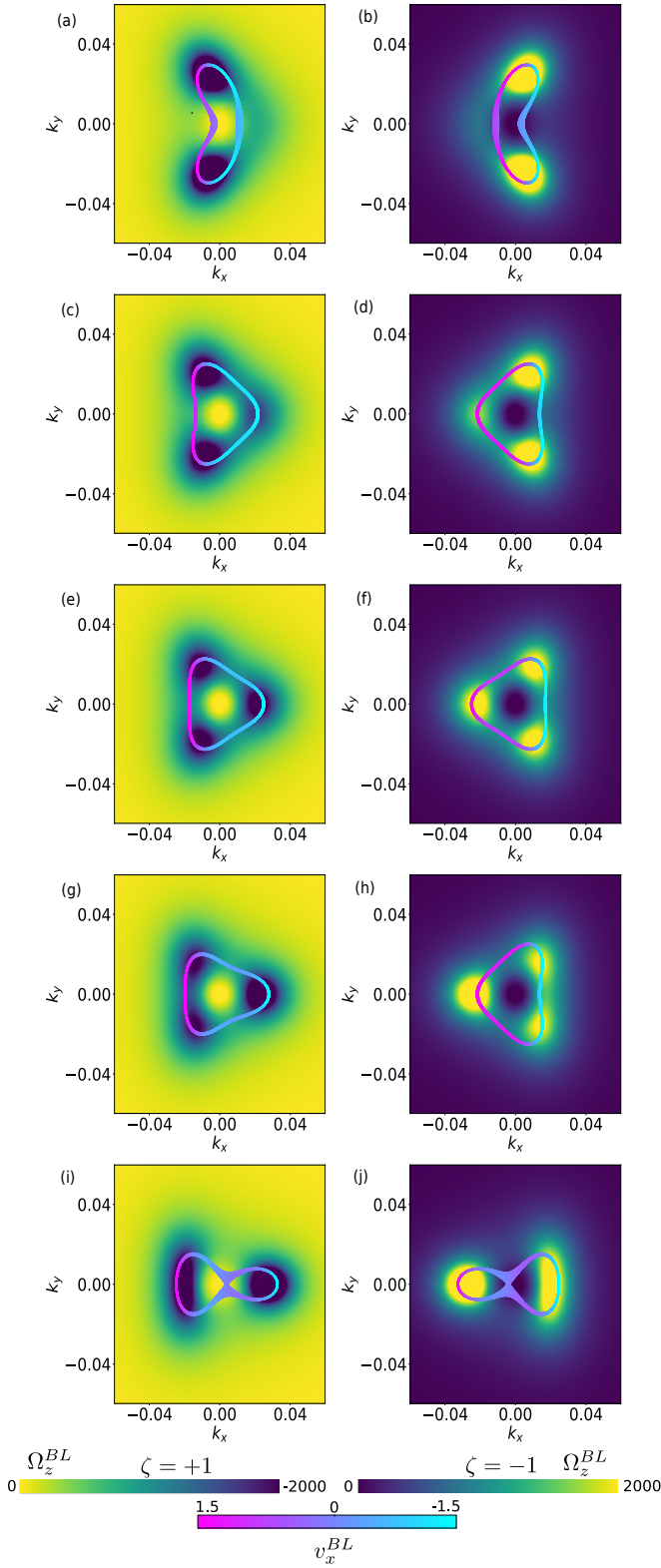


Figure 3. The evolution of BC and Fermi surface in BL graphene (23) with strain w for warping $\lambda_1 = \lambda_2 = \lambda_3 = \lambda = 0.001\text{eV}\cdot\text{\AA}^2$. Left column: The BC $\Omega_z^{BL}(\mathbf{k}, \zeta = +1)$ and $v_x^{BL}(\mathbf{k}, \zeta = +1)$ over the Fermi surface of BL graphene (a) $w = -3m$, (c) $w = -m$, (e) $w = 0$, (g) $w = m$ and (i) $w = 3m$ are shown. Right column: We repeat the same set of calculations for $\zeta = -1$ valley. The parameters (in the units of eV) used are $\Delta_g = 0.06\text{eV}$, $m = 0.008\text{eV}\cdot\text{\AA}^2$, and $v = 0.5\text{eV}\cdot\text{\AA}$. The Fermi surface is plotted for the constant energy $E = -0.04\text{ eV}$.

metry. In order to study the BC mediated transport properties, one has to break the inversion symmetry by applying an external electric field perpendicular to the layers. This reduces the symmetry of the system from D_{3d} to C_{3v} , and creates a gap Δ_g as well as finite BC. The application of a uniaxial strain further reduces the symmetry of the point group to C_v . The low energy Hamiltonian for an inversion broken BL graphene in the presence of a uniaxial strain is expressed below as [29]

$$\mathcal{H}_0^{BL}(\mathbf{k}) = \frac{\Delta_g}{2}\sigma_z + \left(-\frac{1}{2m}(k_y^2 - k_x^2) + \zeta vk_x + \omega\right)\sigma_x - \left(\frac{1}{m}k_x k_y + \zeta vk_y\right)\sigma_y, \quad (22)$$

where v denotes the Fermi velocity related to the skew hopping between the layers, ζ is the valley index and m represents the effective mass dependent on the coupling between the layers. Here, the effect of strain is coming into the Hamiltonian via ω ($= A_3 - A_0$) where A_3 and A_0 are pseudogauge fields. Similar to the ML case, we add trigonal warping terms to the above Hamiltonian to study its effect. The strained-warped BL graphene Hamiltonian takes the following form

$$\begin{aligned} \mathcal{H}^{BL}(\mathbf{k}) = & \frac{\Delta_g}{2}\sigma_z + \left(-\frac{1}{2m}(k_y^2 - k_x^2) + (\lambda_1 k_y^2 - \lambda_2 k_x^2) \right. \\ & \left. + \zeta vk_x + \omega\right)\sigma_x - \left(\frac{1}{m}k_x k_y + \zeta vk_y - 2\zeta\lambda_3 k_x k_y\right)\sigma_y \\ = & \mathbf{N}_{\mathbf{k}} \cdot \boldsymbol{\sigma} \end{aligned} \quad (23)$$

with $\mathbf{N}_{\mathbf{k}} = \{\mathbf{N}_{1\mathbf{k}}, \mathbf{N}_{2\mathbf{k}}, \mathbf{N}_{3\mathbf{k}}\} = \{(\lambda_1 - \frac{1}{2m})k_y^2 + (\frac{1}{2m} - \lambda_2)k_x^2 + \zeta vk_x + \omega, (2\zeta\lambda_3 - \frac{1}{m})k_x k_y - \zeta vk_y, \frac{\Delta_g}{2}\}$. The energy dispersion of the Hamiltonian given in Eq. (23) can be obtained as

$$E^{BL}(\mathbf{k}) = |\mathbf{N}_{\mathbf{k}}| = \pm \sqrt{\mathbf{N}_{1\mathbf{k}}^2 + \mathbf{N}_{2\mathbf{k}}^2 + \mathbf{N}_{3\mathbf{k}}^2}. \quad (24)$$

Note that in Eq. (23), the warping terms are quadratic in momentum, and hence could be absorbed in the already present quadratic momentum terms which indicate interlayer coupling. In this way, the effective masses associated with k_x^2 , k_y^2 and $k_x k_y$ terms are renormalized. Therefore, we can comment at the outset that addition of warping might not affect the system substantially as compared to strain in the ML graphene.

Considering C_3 symmetric warping ($\lambda_1 = \lambda_2 = \lambda_3 = \lambda \neq 0$), the BC for strained BL graphene given in Eq. (23) can be calculated as

$$\Omega_z^{BL}(\mathbf{k}, \zeta) = \mp \frac{\Delta_g \left[A(\lambda, k_x)A(\lambda\zeta, k_x) + B(\lambda, k_y)B(\lambda\zeta, k_y) \right]}{4(E^{BL}(\mathbf{k}))^3} \quad (25)$$

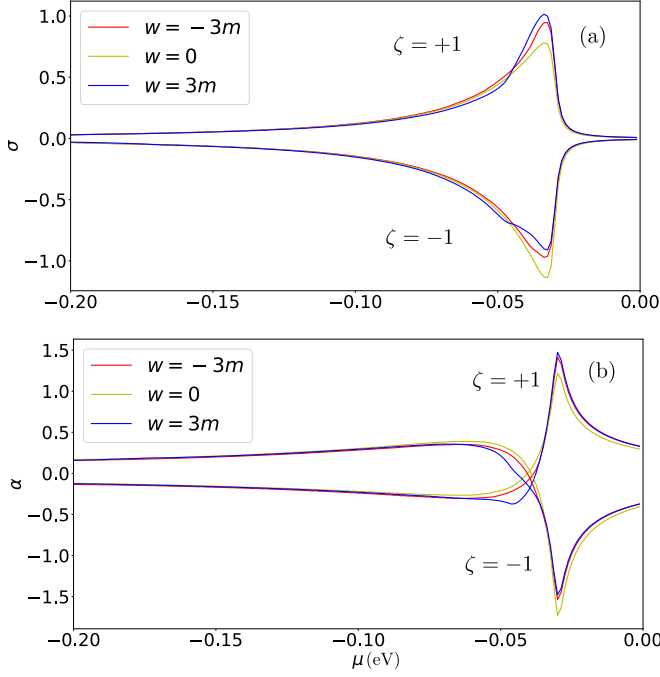


Figure 4. Valley responses of (a) MH (in the unit of $10^2 e^2/\hbar$), (b) MN (in the unit of $10^{-1} ek_B/\hbar$) conductivities in BL graphene with $\Delta U = 0.01$ eV, and $k_B T = 0.001$ eV for $w = -3m, 0, 3m$. All other parameters are kept same as that of in Fig. 3. The prominent and asymmetric valley responses in presence of strain for BL graphene are markedly different from the symmetric responses for ML graphene.

with $A(x, k_x) = \frac{k_x}{m} - 2xk_x + \zeta v$, $B(x, k_y) = \frac{k_y}{m} - 2xk_y$, where $-(+)$ represents conduction (valence) band. The velocity $v_x^{BL}(\mathbf{k}, \zeta)$ takes the form

$$v_x^{BL}(\mathbf{k}, \zeta) = \pm \frac{A(\lambda, k_x)\mathbf{N}_{1\mathbf{k}} - B(\lambda\zeta, k_y)\mathbf{N}_{2\mathbf{k}}}{E^{BL}(\mathbf{k})}. \quad (26)$$

A close inspection suggests that the strain factor w does not appear in the numerator of BC for BL graphene unlike the ML graphene where warping factors λ 's come as corrections over the strain factors $v_1 v_2$. The strain factor comes in the denominator of BC through the energy of the BL graphene. Therefore, the evolution of BC with strain for BL graphene will be significantly different from ML graphene.

The evolution of the $\Omega_z^{BL}(\mathbf{k}, \zeta)$, $v_x^{BL}(\mathbf{k}, \zeta)$ and Fermi surface under strain for valley $\zeta = +1$ and valley $\zeta = -1$ are shown in left and right column of Fig. 3, respectively. For $w = 0$, the three leg gapped Dirac cones (one along $k_y = 0$ and the other two symmetrically placed around $k_x = 0$ line) are observed at $\theta \rightarrow \theta + 2\pi/3$ with $\theta = 0$ following the C_3 symmetric warping [83]. The BC does not change its sign for the three leg gapped Dirac cones within a given valley. This structure of BC for BL graphene is very different from the ML graphene, where BC around satellite Dirac nodes reverses its sign as compared to the parent Dirac node within a given valley. For $w \leq -3m$, there exist two symmetrically placed Dirac

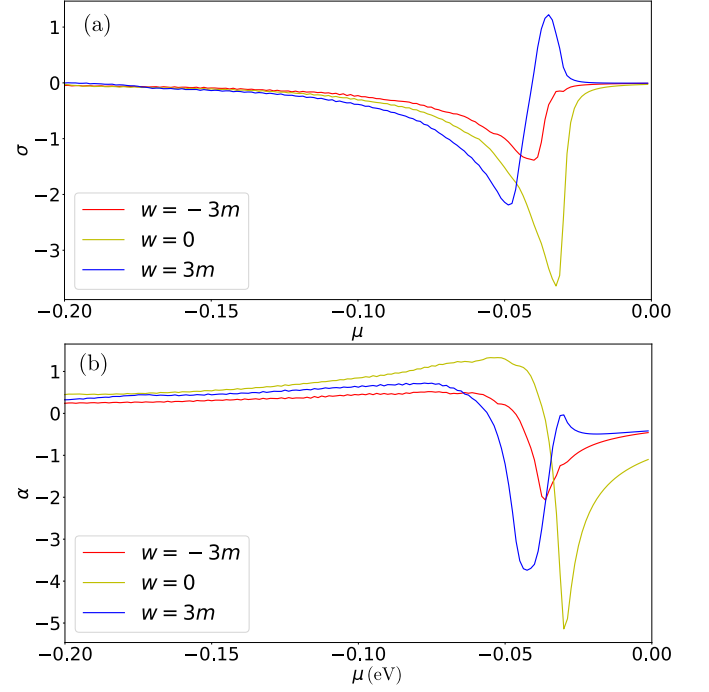


Figure 5. Valley summed (a) MH (in the unit of $10e^2/\hbar$), (b) MN (in the unit of $10^{-2} ek_B/\hbar$) conductivities in BL graphene for $w = -3m, 0, 3m$. The transport behavior changes with strain substantially. We consider the same parameters as used in Fig. 4.

cones around $k_y = 0$ line, while two cones appears on the $k_y = 0$ line for $w \geq 3m$. The threefold rotational symmetry is lost in the presence of uniaxial strain. Interestingly, the Fermi surface is also deformed for the strained case from its unstrained triangular distribution. To be precise, a singly connected Fermi surface for the unstrained case splits into disconnected ones for sufficiently large values of strain. The shape and orientation of the Fermi surfaces appear to be different for larger strain in opposite valleys, which leads to non-identical MH responses in these valleys.

We now investigate the MH and MN conductivities for the individual valleys as shown in Fig. 4 (a) and (b), respectively. The unstrained case leads to asymmetric response in the valleys which is markedly different from ML strained graphene without warping. Upon inclusion of strain, we find that the positive MH responses for the valley $\zeta = +1$ is more pronounced than the negative responses for the other valley $\zeta = -1$. This is due to the fact that activated momenta over the Fermi surface do not have exactly opposite BC in terms of their magnitudes and sign. Moreover, the peak or dip of MHC do not appear at the same chemical potential μ . The Fermi surface distribution strongly depends on valley as well as strain explaining the above observation for MH responses. Therefore, valley polarized transport can in principle be possible like ML strained graphene.

The total valley integrated Magnus responses for BL

graphene are shown in Fig. 5 by varying strain parameter w . For negative values of strain parameter i.e., $w < 0$, MH conductivity always acquires negative values and a dip appears at a certain μ value. The height of the dip increases and its position moves toward $\mu \rightarrow 0$ with decreasing negative strain. On the other hand, by changing the sign of strain i.e., $w > 0$, the dip structure of MH conductivity gets bifurcated into a dip and peak structure. The valley polarized structure of MH responses can explain these observations. We notice qualitatively similar response in MN conductivity.

In summary, for bilayer graphene, we find that strain enhances asymmetry between the valley polarized contribution, resulting in distinct transport signatures for positive and negative strain as compared to the unstrained bilayer graphene.

C. Hexagonal warped topological insulator

We consider the two-dimensional surface Hamiltonian of a TRS invariant TI namely, Bi_2Te_3 , hosting a unique Fermi surface that encloses an odd number of Dirac cones in the surface Brillouin zone. The spin-orbit coupling that is the linear order term in k leads to the band inversion in this system. The minimal two band model contains cubic terms in k in addition to the linear terms in k . This warping can be considered as a counterpart of cubic Dresselhaus spin-orbit coupling term. We note that hexagonal warping incorporates one order higher momentum coupling than the trigonal warping terms. This further allows us to investigate the non-trivial effects of this term that are not captured by the trigonal warping terms.

Considering the threefold rotation C_3 around the z axis and mirror symmetry M : $x \rightarrow -x$, the low-energy model around the gapless Γ point thus reads [31]

$$H^{HW}(\mathbf{k}) = E_0(\mathbf{k}) + v(k_x\sigma_y - k_y\sigma_x) + \frac{\lambda}{2}(k_+^3 + k_-^3)\sigma_z, \quad (27)$$

with $E_0(k) = \frac{k^2}{2m^*}$ causes the particle-hole asymmetry. Dirac velocity v can be considered k independent without loss of generality. Here $k_{\pm} = k_x \pm ik_y$ and λ is the strength of hexagonal warping.

The energy spectrum becomes

$$E^{HW}(\mathbf{k}) = E_0(\mathbf{k}) \pm \sqrt{v^2k^2 + \lambda^2k^6 \cos \phi}, \quad (28)$$

where $\phi = \arctan \frac{k_y}{k_x}$. Using Eq. (18), the BC and x -component of the velocity for the above Hamiltonian can be obtained as

$$\Omega_z^{HW}(\mathbf{k}) = \pm \frac{\lambda v^2(3k_xk_y^2 - 2k_x^3)}{2(v^2k^2 + \lambda^2k^6 \cos \phi)^{\frac{3}{2}}} \quad (29)$$

$$v_x^{HW}(\mathbf{k}) = \frac{k_x}{m^*} \pm \frac{2v^2k_x + \lambda^2k^3k_y^2 + 6\lambda^2k^4k_x \cos \phi}{2\sqrt{v^2k^2 + \lambda^2k^6 \cos \phi}}. \quad (30)$$

where $+$ ($-$) represents conduction (valence) band. The band structure is sixfold symmetric under $\phi \rightarrow \phi + 2\pi/6$. It is clear from the Eq. (29) that the BC is zero in the absence of warping. The band structure is sixfold symmetric under $\phi \rightarrow \phi + 2\pi/6$. The BC distribution with different strength of warping parameter is depicted in Fig. 6. The BC always shows a snowflake like distribution irrespective of the strength of warping. However, the BC acquires substantially large value around the Γ point with increasing λ as also suggested from Eq. (29). Moreover, it reverses sign between two subsequent interval $2n\pi/6 \rightarrow 2(n+1)\pi/6$. On the other hand, the shape of the Fermi surface changes with warping. Specifically, for small warping the Fermi surface takes circular shape. With increasing warping strength, it becomes non-circular with relatively sharp tips extending along high symmetry direction and curves inward in between. Such transformation of Fermi surface from circular to snowflake would initiate interesting transport behavior which we discuss below.

The MH and MN conductivities as a function of chemical potential for different strengths of warping parameter are shown in Fig. 7 (a) and (b), respectively. We find that the magnitude of the MH responses are increasing as well as become more pronounced and sharp with the increase of warping strength. In addition, the position of the dips (peaks) in MH (MN) conductivities moves toward $\mu = 0$ with increasing λ . Moreover, the negative sign of MH conductivity appears because of the majority of negative BC over the activated momentum modes in the Fermi surface.

D. Weyl semimetals

Going beyond the 2D systems, we will now calculate MH responses in 3D WSMs which can be thought of as a 3D analogue of graphene [84]. The low-energy effective Hamiltonian describing the Weyl node with topological charge n and chirality ζ is written as [44, 85–87]

$$H_{\mathbf{k}}^{\zeta} = C_{\zeta}(k_z - \zeta Q) + \zeta \alpha_n \boldsymbol{\sigma} \cdot (\mathbf{n}_{\mathbf{k}} - \zeta \mathbf{e}). \quad (31)$$

where $\zeta = \pm 1$, $k_{\perp} = \sqrt{k_x^2 + k_y^2}$, $\phi_k = \arctan(k_y/k_x)$ and $\mathbf{e} = (0, 0, Q)$. The Weyl nodes of opposite chirality are shifted by an amount $\pm Q$ in momentum space due to broken TRS. C_{ζ} indicates the tilt parameter associated with Weyl node with chirality ζ . Here, $\boldsymbol{\sigma} = \{\sigma_x, \sigma_y, \sigma_z\}$ and $\mathbf{n}_{\mathbf{k}} = \{\alpha_n k_{\perp}^n \cos(n\phi_k), \alpha_n k_{\perp}^n \sin(n\phi_k), vk_z\}$. The factor α_n bears the connection to the Fermi velocity. v is equivalent to the velocity associated with z -direction. For the sake of simplicity, we consider $Q = 0$ and take into account the Weyl nodes of opposite chirality separately. For $C_{\zeta} = 0$, electron and hole bands touch at the Weyl point leading to a point-like Fermi surface. When the magnitude of the tilt parameter is small enough i.e., $|C_{\zeta}|/v \ll 1$, the Fermi surface is still point-like, and is characterized as the type-I Weyl node. With the increase

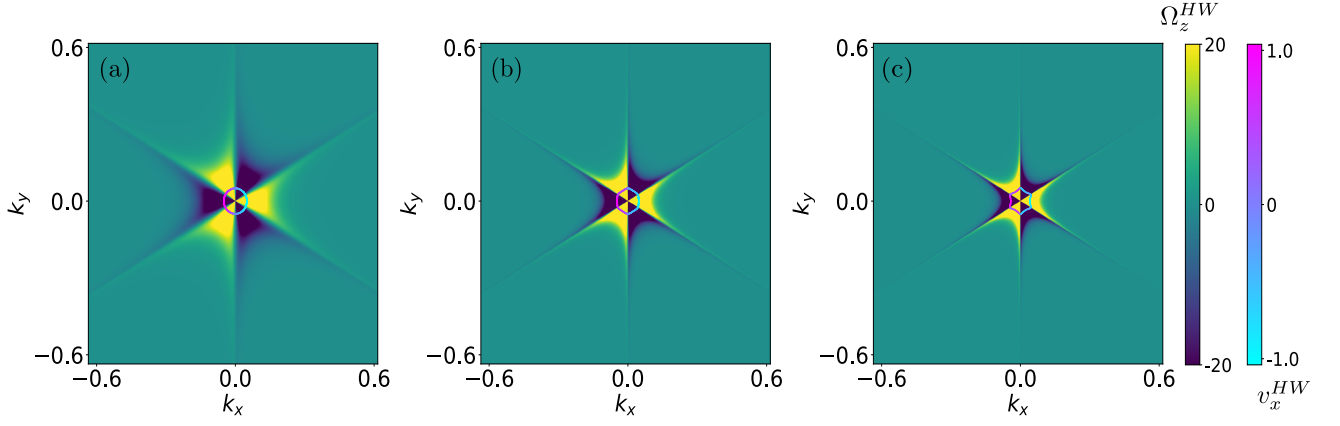


Figure 6. Evolution of BC and Fermi surface, calculated from Eq. (27), with different warping strengths (a) $\lambda=50 \text{ eV}\cdot\text{\AA}^3$, (b) $\lambda=200 \text{ eV}\cdot\text{\AA}^3$ and (c) $\lambda=400 \text{ eV}\cdot\text{\AA}^3$ are shown. Fermi surface is plotted for $E=-0.05 \text{ eV}$. We note that for $\lambda=50 \text{ eV}\cdot\text{\AA}^3$, the Fermi surface remains circular, which gradually evolves to hexagonal shape with increasing λ . We consider $v=1 \text{ eV}\cdot\text{\AA}$ and $E_0=0$ in our calculation.

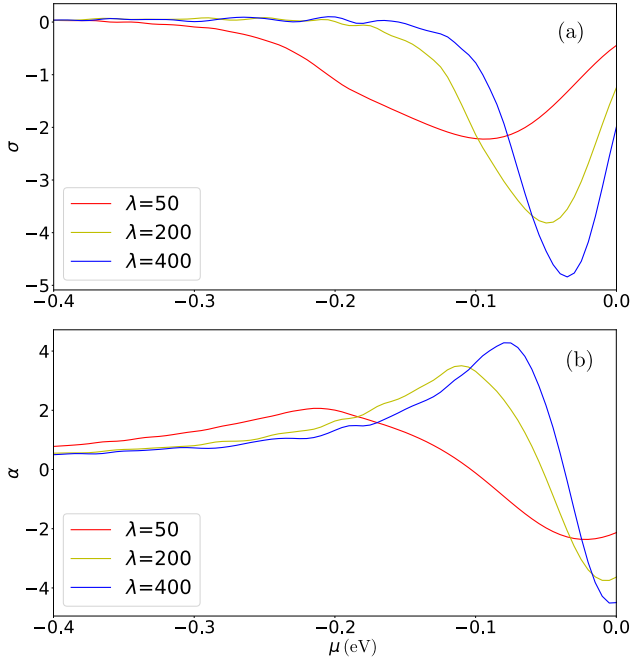


Figure 7. (a) MH (in the unit of $10^{-2}e^2/h$) and (b) MN (in the unit of $10^{-4}ek_B/h$) conductivities as a function of chemical potential for different warping strength $\lambda = 50, 200$ and $400 \text{ eV}\cdot\text{\AA}^3$ are depicted. The parameters used are $v=1 \text{ eV}\cdot\text{\AA}$, $\Delta U = 0.01 \text{ eV}$, and $k_B T = 0.001 \text{ eV}$.

of C_ζ , electron and hole pockets now appear at the Fermi surface for $|C_\zeta|/v \gg 1$ leading to a distinct phase, which is designated as a type-II Weyl node. In this work, we consider two types of tilt configuration for the WSM: i) chiral tilt i.e., $C_+ = -C_-$, and ii) achiral tilt i.e., $C_+ = C_-$.

Now the energy dispersion of the multi-Weyl node with $\zeta = +1$ is given by

$$E^{WSM}(\mathbf{k}, \zeta) = C_\zeta k_z \pm \epsilon_{\mathbf{k}} \quad (32)$$

where $\epsilon_{\mathbf{k}} = \sqrt{\alpha_n^2 k_\perp^{2n} + v^2 k_z^2}$ and $+$ ($-$) represents conduction (valence) band. It is now clear that the dispersion around a Weyl node with $n = 1$ is isotropic in all momentum directions. On the other hand, for $n > 1$, we find that the dispersion around a double (triple) Weyl node becomes quadratic (cubic) along both k_x and k_y directions whereas varies linearly with k_z .

Using Eq. (18), the explicit form of z -component BC associated with the multi-Weyl node can be written as

$$\Omega_z^{WSM}(\mathbf{k}, \zeta) = \pm \frac{1}{2} \frac{\zeta n^2 v \alpha_n^2 k_\perp^{2n-2}}{\epsilon_{\mathbf{k}}^3} k_z. \quad (33)$$

It is clear from the Eq. (33) that, similar to energy dispersion, the BC is isotropic in all momentum directions for single WSM whereas it becomes anisotropic for WSMs with $n > 1$ i.e., for double WSM ($n = 2$) and triple WSM ($n = 3$) due to the presence of k_\perp^{2n-2} factor and topological charge n . Moreover, the BC reverses its sign, retaining the magnitude same, for Weyl nodes of opposite chiralities $\Omega_z^{WSM}(\mathbf{k}, \zeta = +1) = -\Omega_z^{WSM}(\mathbf{k}, \zeta = -1)$. The behavior of BC for both untilted ($C_\zeta = 0$) and tilted ($C_\zeta \neq 0$) multi-Weyl node with $\zeta = +1$ are shown in Fig. 8. With increasing the topological charge n , the single positive and negative lobe of BC gets divided into one pair of lobes. These lobes for $n = 2$ and 3 are deformed with respect to that of $n = 1$. The separation between these lobes increases over the $k_z = 0$ line. The BC changes sign with the chirality of the Weyl node for all WSMs as indicated in Eq. (33). However, the BC is identical in both tilted and untilted WSMs because the tilt does not effect BC. On the other hand, in contrast to BC, the Fermi surface drastically changes in tilted WSM compared to untilted WSM as shown in Fig. 8.

The x -component of the quasi-particle velocity associated with the multi-Weyl node is given by

$$v_x^{WSM}(\mathbf{k}, \zeta) = \frac{k_x n \alpha_n^2 k_\perp^{2n-2}}{\epsilon_{\mathbf{k}}}. \quad (34)$$

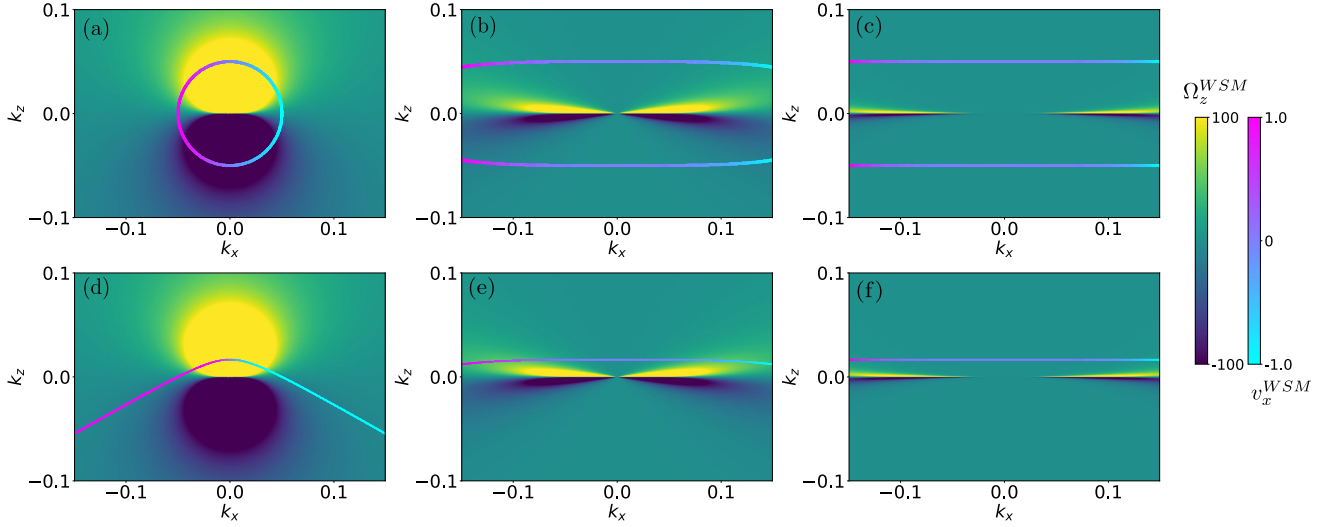


Figure 8. The distribution of the BC and the Fermi surfaces, calculated from Eq. (31), in (a) [(d)] single Weyl node with $n = 1$, (b) [(e)] double Weyl node with $n = 2$ and (c) [(f)] triple Weyl node with $n = 3$ for untitled case i.e., $C_+ = 0$ [tilted case i.e., $C_+ = 2.0$] are shown. The Fermi surface is calculated for $E = -0.05$ eV with $v = 1$ eV·Å. The deformation of BC is clearly observed with increasing non-linearity and anisotropy in the WSM.

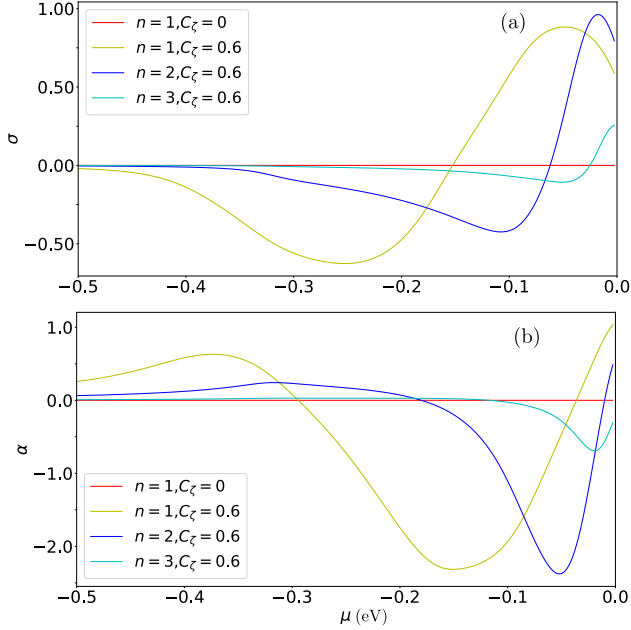


Figure 9. (a) MH (in the unit of $10e^2/h$) and (b) MN (in the unit of ek_B/h) conductivities are shown for tilted and untitled Weyl nodes with $\zeta = +1$. We consider $v = 1$ eV·Å, $\Delta U = 0.01$ eV, and $k_B T = 0.001$ eV. We observe that the untitled Weyl node with $C_+ = 0$ (tilted Weyl node with $C_+ = 0.6$) results in null (substantial) Magnus responses. We note that MH and MN conductivities are exactly opposite at two opposite Weyl nodes with $\zeta = +1$ and -1 owing to the anti-symmetric nature of BC (Eq. (33)).

A close inspection suggests that x -component of the velocity is also independent of the tilt parameter C_ζ (chirality ζ) like (unlike) the BC. Therefore, the effect of the

tilt is only incorporated by the Fermi surface properties. The Fermi surface for $n = 1$ case is circular in shape that gets elongated along k_x direction with increasing n . In the $k_x - k_z$ plane, Fermi surface does not close that is in accordance with the non-point like nature of Fermi surface for tilted WSM. With increasing topological charge n , Fermi surface gets flattened. Therefore, tilt and non-linear dispersion imprint their signature in the transport through Fermi surface properties.

The numerically computed MH responses for single, double and triple Weyl node as a function of μ are shown in Fig. 9. Interestingly, we find that both MH and MN conductivities vanish identically for untitled Weyl node. This is due to the fact that, for a given untitled Weyl node, the positive and negative BC for the activated momentum modes over the Fermi surface are equal, which results in a complete cancellation. This situation remarkably changes in the presence of tilted Weyl node. In this case, the positive and negative BC for the activated momentum modes over the Fermi surface are unequal, and therefore, do not cancel each other completely.

The MH conductivity of a tilted WSM, considering the contribution from two opposite chirality nodes, is given by $\sigma = \sum_\zeta G(\mu)\zeta C_\zeta$, where $G(\mu)$ is μ dependent part of transport coefficient associated with individual Weyl node. For a pair of Weyl nodes at same energy E_0 such that $G(\mu = E_0) = G_0$, the MHE is only finite when relative sign of the tilt parameter between them is opposite, referring to the chiral tilt configuration ($C_+ = -C_-$). On the other hand, the MHE vanishes in the absence of tilt ($C_+ = C_- = 0$), and even in the presence of achiral tilt ($C_+ = C_-$) of the Weyl node. In other words, MH responses from opposite Weyl node add up (cancel each other) leading to a node integrated (polarized) Magnus

(Magnus valley) response in presence of chiral (achiral) tilt. Two Weyl nodes of opposite chirality, residing at two different energies E_+ and E_- , can in principle lead to Magnus valley Hall effect while Weyl nodes exhibit achiral tilt such that $G(\mu = E_+) \neq G(\mu = E_-)$. The MNE follows the same behavior as MHE. This is because the sign of BC is opposite whereas the v_x^{WSM} has same sign for two different nodes of opposite chirality. To shed more light into the tilt mediated MH response, we show the systematic growth of MH conductivity while increasing the tilt strength in Fig. 10.

Therefore, the MH and MN conductivities can become useful probes in distinguishing tilted WSM from an untilted WSM in experiments. We also notice that the responses for $n = 1$ single WSM is found to be most prominent as compared to the WSMs with $n > 1$. This can be explained as the BC reduces its value for the activated momentum modes over the Fermi surface. Moreover, the MH responses decrease as the Fermi surface becomes more flattened for mWSMs. Another interesting feature, coming out from Eq. (33) and (34), is that MH responses from two opposite nodes with chiral (achiral) tilt simply add up (cancel each other) leading to a finite node integrated (polarized) transport coefficients similar to the Magnus (Magnus valley) responses for ML graphene in presence (absence) of warping. From low energy model, it can be shown that the node integrated MH responses are proportional to that of a single tilted Weyl node. All these findings together refer to very interesting Magnus transport properties of WSM in general.

It is pertinent to discuss the anomalous Hall effect that will present alongside with the MHE for the TRS broken WSM as far as the first order responses are concerned. The anomalous Hall conductivity for type-I mWSM is found to be $\sigma' \propto n\Delta k$, where Δk is the separation between two Weyl nodes in momentum space of opposite chirality [64, 88]. On the other hand, the MHE in type-I mWSM ($|C_\zeta/v| \ll 1$) for a given chemical potential can be analytically found as $\sigma \propto n\frac{\Delta U}{v}$. It is clear from the above expressions that the intrinsic AHE increases with increasing the k -space separation between Weyl nodes while remains insensitive to the tilt parameter. By contrast, the magnitude of MH conductivity increases with increasing the built-in electric field. Using the above expressions, one can in general find $\frac{\sigma}{\sigma'} \propto \frac{\Delta U}{v\Delta k}$ (in an arbitrary unit) for type-I WSM. Since this comparison is based on the low-energy model of mWSM, one should consider the lattice model to make a correct estimate of $\frac{\sigma}{\sigma'}$. In addition, we would like to point out that the intrinsic linear AHE can in principle be found to be quantized while MHE is not expected to exhibit quantized response [89].

IV. CONCLUSIONS

In conclusion, we first investigate the effect of strain and warping on MHE and MNE in ballistic regime for 2D

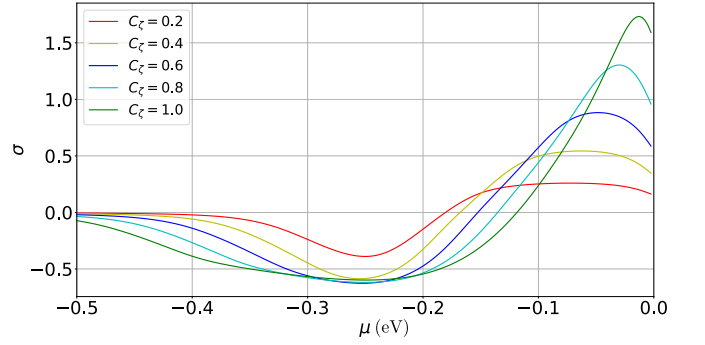


Figure 10. (a) MH (in the unit of $10e^2/h$) conductivity is shown for different strengths of the tilting parameter (C_+) for fixed $n = 1$. Gradual increase in the response is observed with increasing tilt strength C_+ . All other parameters are kept same as mentioned in Fig. 9.

topological systems such as ML, BL graphene and surface states of TIs. We find that in strained ML graphene system without warping, the total Magnus responses are zero after summing over the valleys because the contribution from the each valley cancels with each other. One instead obtains Magnus valley Hall and Magnus valley Nernst effects from the valley polarized contribution. Interestingly, we find that the warping leads to finite total Magnus responses as BC contributions from each valley to Magnus responses are unequal and do not cancel with each other for the asymmetric nature of Fermi surface shape. The magnitude of the total Magnus responses is found to increase with increasing the strength of warping parameter. For BL graphene, strain enhances asymmetry between the valley polarized contribution resulting in distinct transport signatures for positive and negative strain, while the effect of warping remains minimal. In the case of surface states of TI, we find that the magnitude of both MH and MN conductivities enhance with increasing the hexagonal warping strength.

Going beyond 2D, we study Magnus responses in ballistic regime for 3D Weyl semimetals using low-energy model to probe the effect of tilt and anisotropic nonlinear dispersion. In particular, we find that the MHE is identically zero for each Weyl node without tilt, whereas for tilted WSMs, Magnus responses coming from the nodes acquire finite values. Notably, MH responses from opposite Weyl node add up (cancel each other) leading to a node integrated (polarized) Magnus (Magnus valley) response in presence of chiral (achiral) tilt. The magnitude of both MH and MN conductivities increase with increasing the tilt parameter of the Weyl nodes. Moreover, with increasing the topological charge associated with Weyl node, the Magnus responses get suppressed. This key feature can be a useful probe in distinguishing untilted (type-I), tilted (type-I or type-II) WSM and the non-linearity in the dispersion through experiments. Moreover, from the application point of view, such MH responses can pave the way for a new generation of current rectification devices where the alternating-current

signal is converted into a direct-current signal. This is due to the fact that linear Hall effects, the transverse MH voltage (say in y -direction) is developed due to the Magnus velocity of the carriers having positive longitudinal velocity ($v_x > 0$) only.

Related to the experimental realization of MH response in 3D, we would like to first point out that the bulk quantum Hall effect has been realized earlier in quasi-2D systems [91–93]. Recently, 3D systems, such as ZrTe_5 , HfTe_5 , and Cd_3As_2 have been shown to exhibit quantum Hall effect in experiments [94–97]. Moreover, non-linear Hall effect has already been experimentally observed in bilayer non-magnetic quantum material WTe_2 [15], in few layer of WTe_2 [98], and in type-II WSM at room temperature [99]. In light of the above experiments, it is in principle possible to extend the non-linear Hall effect setup, fabricated in 2D, to 3D platforms, where MHE can be experimentally observed. For example, 2D systems can be stacked together in order to form quasi-2D / 3D structure over which multi-terminal Hall measurements can be performed. In the case of MHE, the choice of suitable gate potentials, causing the built-in electric field become very important to generate the appropriate transverse Hall voltage.

In contrast to the linearized model we use in this work,

a real mWSM may contain Weyl nodes with different tilt with respect to one another as well as number of pair of nodes can be greater than one. One of the interesting extensions of this work would be to implement the MH responses calculation on a real mWSM material using DFT or at least on a lattice model in order to directly compare with the experiments. For this purpose, one can perform a four terminal Landauer-Büttiker conductance calculation [100] on a lattice. Following our theoretical analysis on mWSMs, we expect MH responses to be negligible for materials like NbAs, TaAs, which have symmetric untitled Weyl cones. On the other hand, type-II Weyl materials ($\text{MoTe}_2, \text{WTe}_2$) can show substantial MH responses. Moreover, investigating MH responses in twisted BL graphene would be an interesting direction which we leave for future study.

ACKNOWLEDGMENTS

S.N. acknowledges the National Science Foundation Grant No. DMR-1853048. S.K.D would like to thank Ulrike Nitzsche for technical assistance.

-
- [1] E. H. Hall, “On a new action of the magnet on electric currents,” *Am. J. Math.* **2**, 287–292 (1879).
 - [2] Robert Karplus and J. M. Luttinger, “Hall effect in ferromagnetics,” *Phys. Rev.* **95**, 1154–1160 (1954).
 - [3] K. v. Klitzing, G. Dorda, and M. Pepper, “New method for high-accuracy determination of the fine-structure constant based on quantized hall resistance,” *Phys. Rev. Lett.* **45**, 494–497 (1980).
 - [4] F. D. M. Haldane, “Model for a quantum hall effect without landau levels: Condensed-matter realization of the “parity anomaly”,” *Phys. Rev. Lett.* **61**, 2015–2018 (1988).
 - [5] N A Sinitsyn, “Semiclassical theories of the anomalous hall effect,” *J. Phys. Condens. Matter* **20**, 023201 (2007).
 - [6] Naoto Nagaosa, Jairo Sinova, Shigeki Onoda, A. H. MacDonald, and N. P. Ong, “Anomalous hall effect,” *Rev. Mod. Phys.* **82**, 1539–1592 (2010).
 - [7] Cui-Zu Chang, Jinsong Zhang, Xiao Feng, Jie Shen, Zuocheng Zhang, Minghua Guo, Kang Li, Yunbo Ou, Pang Wei, Li-Li Wang, Zhong-Qing Ji, Yang Feng, Shuaihua Ji, Xi Chen, Jinfeng Jia, Xi Dai, Zhong Fang, Shou-Cheng Zhang, Ke He, Yayu Wang, Li Lu, Xu-Cun Ma, and Qi-Kun Xue, “Experimental observation of the quantum anomalous hall effect in a magnetic topological insulator,” *Science* **340**, 167–170 (2013).
 - [8] Chao-Xing Liu, Shou-Cheng Zhang, and Xiao-Liang Qi, “The quantum anomalous hall effect: Theory and experiment,” *Annu. Rev. Condens. Matter Phys.* **7**, 301–321 (2016).
 - [9] Ke He, Yayu Wang, and Qi-Kun Xue, “Topological materials: Quantum anomalous hall system,” *Annu. Rev. Condens. Matter Phys.* **9**, 329–344 (2018).
 - [10] C. L. Kane and E. J. Mele, “Quantum spin hall effect in graphene,” *Phys. Rev. Lett.* **95**, 226801 (2005).
 - [11] Jairo Sinova, Sergio O. Valenzuela, J. Wunderlich, C. H. Back, and T. Jungwirth, “Spin hall effects,” *Rev. Mod. Phys.* **87**, 1213–1260 (2015).
 - [12] Di Xiao, Ming-Che Chang, and Qian Niu, “Berry phase effects on electronic properties,” *Rev. Mod. Phys.* **82**, 1959–2007 (2010).
 - [13] Inti Sodemann and Liang Fu, “Quantum nonlinear hall effect induced by berry curvature dipole in time-reversal invariant materials,” *Phys. Rev. Lett.* **115**, 216806 (2015).
 - [14] Su-Yang Xu, Qiong Ma, Huitao Shen, Valla Fatemi, Sanfeng Wu, Tay-Rong Chang, Guoqing Chang, Andrés M. Mier Valdivia, Ching-Kit Chan, Quinn D. Gibson, Jiadong Zhou, Zheng Liu, Kenji Watanabe, Takashi Taniguchi, Hsin Lin, Robert J. Cava, Liang Fu, Nuh Gedik, and Pablo Jarillo-Herrero, “Electrically switchable berry curvature dipole in the monolayer topological insulator WTe_2 ,” *Nat. Phys.* **14**, 900–906 (2018).
 - [15] Qiong Ma, Su-Yang Xu, Huitao Shen, David MacNeill, Valla Fatemi, Tay-Rong Chang, Andrés M. Mier Valdivia, Sanfeng Wu, Zongzheng Du, Chuang-Han Hsu, Shiang Fang, Quinn D. Gibson, Kenji Watanabe, Takashi Taniguchi, Robert J. Cava, Efthimios Kaxiras, Hai-Zhou Lu, Hsin Lin, Liang Fu, Nuh Gedik, and Pablo Jarillo-Herrero, “Observation of the nonlinear hall effect under time-reversal-symmetric conditions,” *Nature* **565**, 337–342 (2018).
 - [16] Jorge I. Facio, Dmitri Efremov, Klaus Koepernik, Jhih-Shih You, Inti Sodemann, and Jeroen van den Brink,

- “Strongly enhanced berry dipole at topological phase transitions in BiTeI ,” *Phys. Rev. Lett.* **121**, 246403 (2018).
- [17] Xiao-Qin Yu, Zhen-Gang Zhu, Jhih-Shih You, Tony Low, and Gang Su, “Topological nonlinear anomalous nernst effect in strained transition metal dichalcogenides,” *Phys. Rev. B* **99**, 201410 (2019).
- [18] Z. Z. Du, C. M. Wang, Hai-Zhou Lu, and X. C. Xie, “Band signatures for strong nonlinear hall effect in bilayer WTe_2 ,” *Phys. Rev. Lett.* **121**, 266601 (2018).
- [19] Z. Z. Du, C. M. Wang, Shuai Li, Hai-Zhou Lu, and X. C. Xie, “Disorder-induced nonlinear hall effect with time-reversal symmetry,” *Nat. Commun.* **10** (2019), 10.1038/s41467-019-10941-3.
- [20] Z. Z. Du, Hai-Zhou Lu, and X. C. Xie, “Perspective: Nonlinear hall effects,” (2021), [arXiv:2105.10940](https://arxiv.org/abs/2105.10940).
- [21] Carmine Ortix, “Nonlinear hall effect with time-reversal symmetry: Theory and material realizations,” *Adv. Quantum Technol.* **4**, 2100056 (2021).
- [22] Michał Papaj and Liang Fu, “Magnus hall effect,” *Phys. Rev. Lett.* **123**, 216802 (2019).
- [23] Debottam Mandal, Kamal Das, and Amit Agarwal, “Magnus nernst and thermal hall effect,” *Phys. Rev. B* **102**, 205414 (2020).
- [24] Xiaofeng Qian, Junwei Liu, Liang Fu, and Ju Li, “Quantum spin hall effect in two-dimensional transition metal dichalcogenides,” *Science* **346**, 1344–1347 (2014).
- [25] Di Xiao, Gui-Bin Liu, Wanxiang Feng, Xiaodong Xu, and Wang Yao, “Coupled spin and valley physics in monolayers of MoS_2 and other group-vi dichalcogenides,” *Phys. Rev. Lett.* **108**, 196802 (2012).
- [26] Jhih-Shih You, Shiang Fang, Su-Yang Xu, Efthimios Kaxiras, and Tony Low, “Berry curvature dipole current in the transition metal dichalcogenides family,” *Phys. Rev. B* **98**, 121109 (2018).
- [27] Edward McCann and Mikito Koshino, “The electronic properties of bilayer graphene,” *Rep. Prog. Phys.* **76**, 056503 (2013).
- [28] A.V. Rozhkov, A.O. Sboychakov, A.L. Rakhmanov, and Franco Nori, “Electronic properties of graphene-based bilayer systems,” *Phys. Rep.* **648**, 1–104 (2016), electronic properties of graphene-based bilayer systems.
- [29] Raffaele Battilomo, Niccolò Scopigno, and Carmine Ortix, “Berry curvature dipole in strained graphene: A fermi surface warping effect,” *Phys. Rev. Lett.* **123**, 196403 (2019).
- [30] Matthew Yankowitz, Jiamin Xue, Daniel Cormode, Javier D. Sanchez-Yamagishi, K. Watanabe, T. Taniguchi, Pablo Jarillo-Herrero, Philippe Jacquod, and Brian J. LeRoy, “Emergence of superlattice dirac points in graphene on hexagonal boron nitride,” *Nat. Phys.* **8**, 382–386 (2012).
- [31] Liang Fu, “Hexagonal warping effects in the surface states of the topological insulator Bi_2Te_3 ,” *Phys. Rev. Lett.* **103**, 266801 (2009).
- [32] Kai-Yu Yang, Yuan-Ming Lu, and Ying Ran, “Quantum hall effects in a weyl semimetal: Possible application in pyrochlore iridates,” *Phys. Rev. B* **84**, 075129 (2011).
- [33] A. A. Burkov, M. D. Hook, and Leon Balents, “Topological nodal semimetals,” *Phys. Rev. B* **84**, 235126 (2011).
- [34] Shuichi Murakami, Satoshi Iso, Yshai Avishai, Masaru Onoda, and Naoto Nagaosa, “Tuning phase transition between quantum spin hall and ordinary insulating phases,” *Phys. Rev. B* **76**, 205304 (2007).
- [35] Shuichi Murakami, “Phase transition between the quantum spin hall and insulator phases in 3d: emergence of a topological gapless phase,” *New J. Phys.* **9**, 356–356 (2007).
- [36] A. A. Burkov and Leon Balents, “Weyl semimetal in a topological insulator multilayer,” *Phys. Rev. Lett.* **107**, 127205 (2011).
- [37] Xiangang Wan, Ari M. Turner, Ashvin Vishwanath, and Sergey Y. Savrasov, “Topological semimetal and fermi-arc surface states in the electronic structure of pyrochlore iridates,” *Phys. Rev. B* **83**, 205101 (2011).
- [38] N. P. Armitage, E. J. Mele, and Ashvin Vishwanath, “Weyl and dirac semimetals in three-dimensional solids,” *Rev. Mod. Phys.* **90**, 015001 (2018).
- [39] A. A. Zyuzin, Si Wu, and A. A. Burkov, “Weyl semimetal with broken time reversal and inversion symmetries,” *Phys. Rev. B* **85**, 165110 (2012).
- [40] Timothy M. McCormick, Itamar Kimchi, and Nandini Trivedi, “Minimal models for topological weyl semimetals,” *Phys. Rev. B* **95**, 075133 (2017).
- [41] G.E. Volovik and M.A. Zubkov, “Emergent weyl spinors in multi-fermion systems,” *Nucl. Phys. B* **881**, 514–538 (2014).
- [42] Yong Xu, Fan Zhang, and Chuanwei Zhang, “Structured weyl points in spin-orbit coupled fermionic superfluids,” *Phys. Rev. Lett.* **115**, 265304 (2015).
- [43] Alexey A. Soluyanov, Dominik Gresch, Zhijun Wang, QuanSheng Wu, Matthias Troyer, Xi Dai, and B. Andrei Bernevig, “Type-II weyl semimetals,” *Nature* **527**, 495–498 (2015).
- [44] Gang Xu, Hongming Weng, Zhijun Wang, Xi Dai, and Zhong Fang, “Chern semimetal and the quantized anomalous hall effect in HgCr_2Se_4 ,” *Phys. Rev. Lett.* **107**, 186806 (2011).
- [45] Chen Fang, Matthew J. Gilbert, Xi Dai, and B. Andrei Bernevig, “Multi-weyl topological semimetals stabilized by point group symmetry,” *Phys. Rev. Lett.* **108**, 266802 (2012).
- [46] Ki-Seok Kim, Heon-Jung Kim, and M. Sasaki, “Boltzmann equation approach to anomalous transport in a weyl metal,” *Phys. Rev. B* **89**, 195137 (2014).
- [47] Pavan Hosur and Xiaoliang Qi, “Recent developments in transport phenomena in weyl semimetals,” *C. R. Phys.* **14**, 857–870 (2013).
- [48] Xiaochun Huang, Lingxiao Zhao, Yujia Long, Peipei Wang, Dong Chen, Zhanhai Yang, Hui Liang, Mianqi Xue, Hongming Weng, Zhong Fang, Xi Dai, and Genfu Chen, “Observation of the chiral-anomaly-induced negative magnetoresistance in 3d weyl semimetal TaAs ,” *Phys. Rev. X* **5**, 031023 (2015).
- [49] Vladimir A. Zyuzin, “Magnetotransport of weyl semimetals due to the chiral anomaly,” *Phys. Rev. B* **95**, 245128 (2017).
- [50] D. T. Son and B. Z. Spivak, “Chiral anomaly and classical negative magnetoresistance of weyl metals,” *Phys. Rev. B* **88**, 104412 (2013).
- [51] A. A. Burkov, “Giant planar hall effect in topological metals,” *Phys. Rev. B* **96**, 041110 (2017).
- [52] A A Burkov, “Chiral anomaly and transport in weyl metals,” *J. Phys. Condens. Matter* **27**, 113201 (2015).
- [53] Yaojia Wang, Erfu Liu, Huimei Liu, Yiming Pan, Longqiang Zhang, Junwen Zeng, Yajun Fu, Miao Wang,

- Kang Xu, Zhong Huang, Zhenlin Wang, Hai-Zhou Lu, Dingyu Xing, Baigeng Wang, Xiangang Wan, and Feng Miao, “Gate-tunable negative longitudinal magnetoresistance in the predicted type-ii weyl semimetal WTe_2 ,” *Nat. Commun.* **7**, 13142 (2016).
- [54] Cheng-Long Zhang, Su-Yang Xu, Ilya Belopolski, Zhu-jun Yuan, Ziquan Lin, Bingbing Tong, Guang Bian, Nasser Alidoust, Chi-Cheng Lee, Shin-Ming Huang, Tay-Rong Chang, Guoqing Chang, Chuang-Han Hsu, Horng-Tay Jeng, Madhab Neupane, Daniel S. Sanchez, Hao Zheng, Junfeng Wang, Hsin Lin, Chi Zhang, Hai-Zhou Lu, Shun-Qing Shen, Titus Neupert, M. Zahid Hasan, and Shuang Jia, “Signatures of the adler–bell–jackiw chiral anomaly in a weyl fermion semimetal,” *Nat. Commun.* **7**, 10735 (2016).
- [55] S. Nandy, Girish Sharma, A. Taraphder, and Sumanta Tewari, “Chiral anomaly as the origin of the planar hall effect in weyl semimetals,” *Phys. Rev. Lett.* **119**, 176804 (2017).
- [56] F. C. Chen, X. Luo, J. Yan, Y. Sun, H. Y. Lv, W. J. Lu, C. Y. Xi, P. Tong, Z. G. Sheng, X. B. Zhu, W. H. Song, and Y. P. Sun, “Planar hall effect in the type-ii weyl semimetal $Td\text{-MoTe}_2$,” *Phys. Rev. B* **98**, 041114 (2018).
- [57] Ratnadwip Singha, Shubhankar Roy, Arnab Pariari, Biswarup Satpati, and Prabhat Mandal, “Planar hall effect in the type-ii dirac semimetal val_3 ,” *Phys. Rev. B* **98**, 081103 (2018).
- [58] Suvendu Ghosh, Debabrata Sinha, Snehasish Nandy, and A. Taraphder, “Chirality-dependent planar hall effect in inhomogeneous weyl semimetals,” *Phys. Rev. B* **102**, 121105 (2020).
- [59] Nitesh Kumar, Satya N. Guin, Claudia Felser, and Chandra Shekhar, “Planar hall effect in the weyl semimetal gdptbi ,” *Phys. Rev. B* **98**, 041103 (2018).
- [60] M. Udagawa and E. J. Bergholtz, “Field-selective anomaly and chiral mode reversal in type-ii weyl materials,” *Phys. Rev. Lett.* **117**, 086401 (2016).
- [61] Fucong Fei, Xiangyan Bo, Rui Wang, Bin Wu, Juan Jiang, Dongzhi Fu, Ming Gao, Hao Zheng, Yulin Chen, Xuefeng Wang, Haijun Bu, Fengqi Song, Xiangang Wan, Baigeng Wang, and Guanghou Wang, “Nontrivial berry phase and type-ii dirac transport in the layered material PdTe_2 ,” *Phys. Rev. B* **96**, 041201 (2017).
- [62] Renato M. A. Dantas, Francisco Peña-Benitez, Bitan Roy, and Piotr Surówka, “Magnetotransport in multi-weyl semimetals: a kinetic theory approach,” *J. High Energy Phys.* **2018** (2018), 10.1007/jhep12(2018)069.
- [63] Tanay Nag and Snehasish Nandy, “Magnetotransport phenomena of type-i multi-weyl semimetals in co-planar setups,” *J. Phys. Condens. Matter* **33**, 075504 (2020).
- [64] Tanay Nag, Anirudha Menon, and Banasri Basu, “Thermoelectric transport properties of floquet multi-weyl semimetals,” *Phys. Rev. B* **102**, 014307 (2020).
- [65] Neil W Ashcroft and N David Mermin, *Solid state physics* (New York: Holt, Rinehart and Winston, 1976).
- [66] John M Ziman, *Electrons and phonons: the theory of transport phenomena in solids* (Oxford university press, 2001).
- [67] Di Xiao, Ming-Che Chang, and Qian Niu, “Berry phase effects on electronic properties,” *Rev. Mod. Phys.* **82**, 1959–2007 (2010).
- [68] Dam Thanh Son and Naoki Yamamoto, “Berry curvature, triangle anomalies, and the chiral magnetic effect in fermi liquids,” *Phys. Rev. Lett.* **109**, 181602 (2012).
- [69] Di Xiao, Yugui Yao, Zhong Fang, and Qian Niu, “Berry-phase effect in anomalous thermoelectric transport,” *Phys. Rev. Lett.* **97**, 026603 (2006).
- [70] Liang Dong, Cong Xiao, Bangguo Xiong, and Qian Niu, “Berry phase effects in dipole density and the mott relation,” *Phys. Rev. Lett.* **124**, 066601 (2020).
- [71] Yang Zhang, Yan Sun, and Binghai Yan, “Berry curvature dipole in weyl semimetal materials: An ab initio study,” *Phys. Rev. B* **97**, 041101 (2018).
- [72] Chuanchang Zeng, Snehasish Nandy, and Sumanta Tewari, “Nonlinear transport in weyl semimetals induced by berry curvature dipole,” *Phys. Rev. B* **103**, 245119 (2021).
- [73] Fernando de Juan, Adolfo G Grushin, Takahiro Morimoto, and Joel E Moore, “Quantized circular photogalvanic effect in weyl semimetals,” *Nature communications* **8**, 15995 (2017).
- [74] Banasree Sadhukhan and Tanay Nag, “Role of time reversal symmetry and tilting in circular photogalvanic responses,” *Phys. Rev. B* **103**, 144308 (2021).
- [75] Rui-Chun Xiao, Zibo Wang, Zhi-Qiang Zhang, Junwei Liu, and Hua Jiang, “Magnus hall effect in two-dimensional materials,” *Chinese Phys. Lett.* **38**, 057301 (2021).
- [76] C. R. Woods, L. Britnell, A. Eckmann, R. S. Ma, J. C. Lu, H. M. Guo, X. Lin, G. L. Yu, Y. Cao, R. V. Gorbachev, A. V. Kretinin, J. Park, L. A. Ponomarenko, M. I. Katsnelson, Yu. N. Gornostyrev, K. Watanabe, T. Taniguchi, C. Casiraghi, H.-J. Gao, A. K. Geim, and K. S. Novoselov, “Commensurate–incommensurate transition in graphene on hexagonal boron nitride,” *Nat. Phys.* **10**, 451–456 (2014).
- [77] Gianluca Giovannetti, Petr A. Khomyakov, Geert Brocks, Paul J. Kelly, and Jeroen van den Brink, “Substrate-induced band gap in graphene on hexagonal boron nitride: Ab initio density functional calculations,” *Phys. Rev. B* **76**, 073103 (2007).
- [78] Fernando de Juan, Mauricio Sturla, and María A. H. Vozmediano, “Space dependent fermi velocity in strained graphene,” *Phys. Rev. Lett.* **108**, 227205 (2012).
- [79] Hualing Zeng, Junfeng Dai, Wang Yao, Di Xiao, and Xiaodong Cui, “Valley polarization in MoS_2 monolayers by optical pumping,” *Nat. Nanotechnol.* **7**, 490–493 (2012).
- [80] Kin Fai Mak, Keliang He, Jie Shan, and Tony F. Heinz, “Control of valley polarization in monolayer MoS_2 by optical helicity,” *Nat. Nanotechnol.* **7**, 494–498 (2012).
- [81] Di Xiao, Wang Yao, and Qian Niu, “Valley-contrasting physics in graphene: Magnetic moment and topological transport,” *Phys. Rev. Lett.* **99**, 236809 (2007).
- [82] Sonja Predin, Paul Wenk, and John Schliemann, “Trigonal warping in bilayer graphene: Energy versus entanglement spectrum,” *Phys. Rev. B* **93**, 115106 (2016).
- [83] Edward McCann and Vladimir I. Fal’ko, “Landau-level degeneracy and quantum hall effect in a graphite bilayer,” *Phys. Rev. Lett.* **96**, 086805 (2006).
- [84] Binghai Yan and Claudia Felser, “Topological materials: Weyl semimetals,” *Annu. Rev. Condens. Matter Phys.* **8**, 337–354 (2017).
- [85] Chen Fang, Matthew J. Gilbert, Xi Dai, and B. Andrei Bernevig, “Multi-weyl topological semimetals sta-

- bilized by point group symmetry,” *Phys. Rev. Lett.* **108**, 266802 (2012).
- [86] Bohm-Jung Yang and Naoto Nagaosa, “Classification of stable three-dimensional dirac semimetals with nontrivial topology,” *Nat. Commun.* **5**, 4898 (2014).
- [87] Bitan Roy, Pallab Goswami, and Vladimir Juričić, “Interacting weyl fermions: Phases, phase transitions, and global phase diagram,” *Phys. Rev. B* **95**, 201102 (2017).
- [88] A. A. Burkov, “Anomalous hall effect in weyl metals,” *Phys. Rev. Lett.* **113**, 187202 (2014).
- [89] Simin Nie, Yan Sun, Fritz B. Prinz, Zhijun Wang, Hongming Weng, Zhong Fang, and Xi Dai, “Magnetic semimetals and quantized anomalous hall effect in eub₆,” *Phys. Rev. Lett.* **124**, 076403 (2020).
- [90] Chandra Shekhar, Nitesh Kumar, V Grinenko, Sanjay Singh, R Sarkar, H Luetkens, Shu-Chun Wu, Yang Zhang, Alexander C Komarek, Erik Kampert, *et al.*, “Anomalous hall effect in weyl semimetal half-heusler compounds rptbi (r= gd and nd),” *Proceedings of the National Academy of Sciences* **115**, 9140–9144 (2018).
- [91] Helin Cao, Jifa Tian, Ireneusz Miotkowski, Tian Shen, Jiuning Hu, Shan Qiao, and Yong P. Chen, “Quantized hall effect and shubnikov–de haas oscillations in highly doped bi₂se₃: Evidence for layered transport of bulk carriers,” *Phys. Rev. Lett.* **108**, 216803 (2012).
- [92] Hidetoshi Masuda, Hideaki Sakai, Masashi Tokunaga, Yuichi Yamasaki, Atsushi Miyake, Junichi Shiogai, Shintaro Nakamura, Satoshi Awaji, Atsushi Tsukazaki, Hironori Nakao, Youichi Murakami, Taka hisa Arima, Yoshinori Tokura, and Shintaro Ishiwata, “Quantum hall effect in a bulk antiferromagnet EuMnBi₂ with magnetically confined two-dimensional dirac fermions,” *Sci. Adv.* **2**, e1501117 (2016).
- [93] Masaki Uchida, Yusuke Nakazawa, Shinichi Nishihaya, Kazuto Akiba, Markus Kriener, Yusuke Kozuka, Atsushi Miyake, Yasujiro Taguchi, Masashi Tokunaga, Naoto Nagaosa, *et al.*, “Quantum hall states observed in thin films of dirac semimetal Cd₃As₂,” *Nature communications* **8**, 2274 (2017).
- [94] Cheng Zhang, Yi Zhang, Xiang Yuan, Shiheng Lu, Jinglei Zhang, Awadhesh Narayan, Yanwen Liu, Huiqin Zhang, Zhuoliang Ni, Ran Liu, Eun Sang Choi, Alexey Suslov, Stefano Sanvito, Li Pi, Hai-Zhou Lu, Andrew C. Potter, and Faxian Xiu, “Quantum hall effect based on weyl orbits in Cd₃As₂,” *Nature* **565**, 331–336 (2018).
- [95] Tian Liang, Jingjing Lin, Quinn Gibson, Satya Kushwaha, Minhao Liu, Wudi Wang, Hongyu Xiong, Jonathan A. Sobota, Makoto Hashimoto, Patrick S. Kirchmann, Zhi-Xun Shen, R. J. Cava, and N. P. Ong, “Anomalous hall effect in ZrTe₅,” *Nat. Phys.* **14**, 451–455 (2018).
- [96] Fangdong Tang, Yafei Ren, Peipei Wang, Ruidan Zhong, John Schneeloch, Shengyuan A. Yang, Kun Yang, Patrick A. Lee, Genda Gu, Zhenhua Qiao, and Liyuan Zhang, “Three-dimensional quantum hall effect and metal–insulator transition in ZrTe₅,” *Nature* **569**, 537–541 (2019).
- [97] S. Galeski, X. Zhao, R. Wawrzyńczak, T. Meng, T. Förster, P. M. Lozano, S. Honnali, N. Lamba, T. Ehmcke, A. Markou, Q. Li., G. Gu, W. Zhu, J. Wosnitza, C. Felser, G. F. Chen, and J. Gooth, “Unconventional hall response in the quantum limit of HfTe₅,” *Nat. Commun.* **11**, 5926 (2020).
- [98] Kaifei Kang, Tingxin Li, Egon Sohn, Jie Shan, and Kin Fai Mak, “Nonlinear anomalous hall effect in few-layer WTe₂,” *Nat. Mater.* **18**, 324–328 (2019).
- [99] Dushyant Kumar, Chuang-Han Hsu, Raghav Sharma, Tay-Rong Chang, Peng Yu, Junyong Wang, Goki Eda, Gengchiao Liang, and Hyunsoo Yang, “Room-temperature nonlinear hall effect and wireless radiofrequency rectification in weyl semimetal TaIrTe₄,” *Nat. Nanotechnol.* **16**, 421–425 (2021).
- [100] M. Büttiker, “Four-terminal phase-coherent conductance,” *Phys. Rev. Lett.* **57**, 1761–1764 (1986).